Nano Research

Open Access

Research Article

Engineering sub-micron axial heterostructures in ZnO-C nanowires by low energy electron irradiation

Joon Kiat Kang[1], Kim Yong Lim[1], Debbie Hwee Leng Seng[2], and Chorng Haur Sow[1]✉

[1] *Department of Physics, National University of Singapore, 2 Science Drive 3, Singapore 117542, Singapore*
[2] *Institute of Materials Research and Engineering, A*STAR (Agency for Science, Technology and Research), #08-03, 2 Fusionopolis Way, Innovis, Singapore 138634, Singapore*

Cite this article: *Nano Research*, **2026**, *19*, 94908866. https://doi.org/10.26599/NR.2026.94908866

ABSTRACT: Carbon-incorporated zinc oxide (ZnO-C) nanowires (NWs) demonstrate an enhanced variety of post-fabrication modification pathways such as electron beam treatment. Using localized low energy electron irradiation in a scanning electron microscope, axial heterostructures with varying defect fluorescence properties were engineered with sub-micron precision in ZnO-C nanowires. The electron-induced modification of the defect fluorescence of four types of nanowires, differentiated by their carbon content and defect fluorescence polarization, were characterized. Spatially extensive fluorescence quenching was observed in nanowires with lower carbon content. In higher carbon content nanowires, localized fluorescence intensity enhancement and color conversion from red to green were observed. In nanowires with an additional polarized emission component, the polarized component exhibited localized quenching independent of the unpolarized component. Additionally, electron beam induced deposition of amorphous carbon was achieved on ZnO-C NWs and found to be controllable by electron irradiation parameters. X-ray photoelectron spectroscopy measurements conducted on nanowire array samples implied that electron irradiation caused the replacement of zinc with carbon atoms. Finally, a method of visualizing electron trajectories through the nanowire by imaging the electron-enhanced fluorescence of surface contamination on the substrate was demonstrated and used to validate trajectories simulated by Monte Carlo simulations.

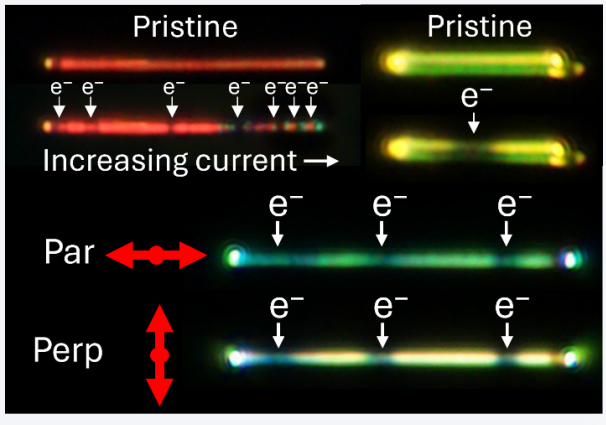

KEYWORDS: defect, fluorescence, engineering, electron, zinc oxide, carbon

1 Introduction

Zinc oxide is a semiconductor with a wide band gap of 3.37 eV corresponding to ultraviolet (UV) energy range, which means that light emission of all visible wavelengths via radiative recombination is accessible with appropriate tuning of intra-band gap defect levels. ZnO also has a strong exciton binding energy of 60 meV, which means that excitonic phenomena are stable at room temperatures, making it a promising material for room temperature optoelectronic device applications. Nominally undoped ZnO exhibits photoluminescence (PL) under UV excitation typically in two bands: a near band edge UV emission between 370 and 375 nm and a broadband green defect emission that is often attributed to oxygen vacancies [1]. ZnO also displays impressive radiation hardness [2] which has been attributed to concomitant annealing during irradiation [3], allowing its properties to be modified post-fabrication via irradiation without excessively damaging the underlying crystal structure. Other attractive properties of ZnO are the low cost of zinc, high electron mobility, optical transparency in the visible band, ease of electron doping, innate piezoelectricity, low biological toxicity, and availability of multiple vapor transport and solution-based fabrication pathways [1, 4–8]. Among solution-based fabrication methods, photon irradiation-activated localized growth of ZnO has also seen notable progress. By using a focused laser to achieve localized heating, spatially selective clusters of ZnO NW have been grown on planar substrates [9, 10] and metallic NWs [11]. Cluster dimensions could also be controlled by tailoring substrate properties [12]. These

Received: March 18, 2026; **Revised:** May 12, 2026
Accepted: May 22, 2026

✉Address correspondence to physowch@nus.edu.sg

focused-laser activated growth methods enabled bottom-up growth patterning by scanning the laser across the substrate in desired patterns [13].

ZnO typically forms in the hexagonal wurtzite crystal structure which is the stable allotrope at room temperatures and pressure [1]. Notably, the structure has a preferential growth direction in the <0001> direction, meaning that ZnO easily forms high aspect ratio nanostructures like NWs. NWs are an especially technologically relevant class of materials due to their advantageous properties. Some properties include large crystalline domains, low density of grain boundaries, long distance order, increased surface sensitivity from high surface area to volume ratio, anisotropy, sensitivity to light, electron confinement, light confinement, size confinement effects, and size- and shape-dependent properties [5, 14, 15]. NW surface facets also often do not exist in their thermodynamic ground state due to the varying kinetic and energetic conditions across different growth methods [16] and are susceptible to post-fabrication morphological modification.

While undoped ZnO already possesses many beneficial properties, impurity doping can introduce a larger variety of properties for additional engineering opportunities. Carbon incorporation in trace amounts introduces carbon-containing defects that alter the photoluminescence properties of carbon-incorporated ZnO (ZnO-C) while retaining the general properties of ZnO. It also causes the material to display a richer variety of irradiation-induced changes for post fabrication modification. Tuning of the carbon concentration during fabrication has been used to modify the near band edge emissions, defect fluorescence, and surface structure of ZnO-C NWs, notably red-shifting the defect fluorescence from the typical green to a deep brownish-red [17]. The photoluminescence of these NWs was also amenable to post-fabrication modification by focused laser treatment [18]. The flow of electrons through ZnO-C was also found to dramatically modify the photoluminescence properties. In the work by Bah et al. [19], the use of ZnO-C NW arrays as electron field emitters enhanced the intensity of both the near band edge emissions and defect emissions. The intensity ratios of near band edge emissions to defect emissions were also increased. In NWs with higher carbon concentration, drastic changes in defect fluorescence color from predominantly red to green, orange, and purple were observed. In the work by Sow et al. [20], the passage of direct current through individual ZnO-C NWs with heterogeneous fluorescence caused both transient and permanent changes in the intensity and color of fluorescence depending on the voltage held across the NW. The fluorescence distribution also transformed from a gradated variation of colors to a punctuated and "bead-like" distribution. Individual beads of colors were also observed to move due to passage of current.

The post-treatment heterogeneous fluorescence observed in the above two works hinted at the possibility that electron interaction with ZnO-C NWs can cause localized modifications. However, due to the limitations of electron treatment via field emission and passage of direct current, controlling the modification location with high spatial precision was not feasible. In this work, the investigation of electron-induced modification of individual ZnO-C NWs and nanobelts (NBs) was extended by employing a scanning electron microscopy (SEM) to perform low energy electron (LEE) treatment with sub-micron spatial resolution. Two major aspects of the SEM enable this. Firstly, the location of electron irradiation can be easily controlled due to the availability of *in-situ* visualization while adjusting the SEM viewport. Secondly, many electron irradiation parameters can be adjusted through SEM operating parameters. In this work, the dependence on electron energy, emission current, probe current, irradiation duration, and magnification at which irradiation was carried out were investigated. It was found that the defect fluorescence in ZnO-C NWs could be modified with better location control than previously achieved, allowing for fluorescence patterning of the NWs with sub-micron precision. Different forms of fluorescence modification were also observed for different types of NWs. Additionally, at longer irradiation durations, electron beam-induced deposition (EBID) of amorphous carbon was observed, causing material outgrowth on NWs whose size, shape, and position could be precisely controlled by SEM operation. X-ray photoelectron spectroscopy (XPS) analysis suggested that electron irradiation of ZnO-C induced the replacement of zinc ions with carbon, following which a mechanism for LEE induced modification of ZnO-C was proposed. Finally, we probe the electron scattering profile in ZnO-C NWs by fluorescence imaging of the underlying silicon substrate.

We distinguish four types of NWs by their defect fluorescence colors under ultraviolet (UV) excitation. Type 1A NWs exhibit a broadband green fluorescence. Type 1B NWs exhibit the same green fluorescence as Type 1A in addition to a 2.2 eV yellow fluorescence that is polarized perpendicular to the long axis of the NW. The polarized fluorescence is emitted from the entire length of the NW. An oriented C_O-V_O defect complex concentrated on the NW surface was deduced to be responsible for the polarized emission after analyzing the partial density of states in tandem with the predicted defect atomic structure [21]. The polarized yellow emission and unpolarized green emission can be visually distinguished by examining the emission through a rotatable linear polarizer. Type 2A NWs exhibit a broadband red fluorescence that is typically lower intensity than the broadband green fluorescence in Type 1A NWs. Type 2B NWs exhibit the same red fluorescence seen in Type 2A NWs in addition to the polarized 2.2 eV yellow fluorescence exhibited by Type 1B NWs.

Type 1A and Type 1B NWs were fabricated in the same batch by chemical vapor deposition with a ZnO:C mass ratio of 1:1. On the other hand, Type 2A and Type 2B NWs were fabricated in a separate batch with a ZnO:C mass ratio of 1:3 and have been shown to contain higher carbon content than Type 1A and Type 1B [17]. Previous computations [17, 22] identified $2C_O$-Zn_i, $3C_O$, $3C_O$-V_{Zn}, C_O-V_O, C_O-Zn_i, and $2C_O$-V_O-Zn_i as energetically viable defects in ZnO-C. Based on the energy transitions in the calculated partial density of states, the defects in Type 1A and Type 1B NWs are dominated by $3C_O$-V_{Zn} (2.20 eV), C_O-V_O (2.22 eV), and C_O-Zn_i (2.31 eV), with Type 1B NWs having a higher concentration of the C_O-V_O capable of emitting polarized light. Type 2A and Type 2B NWs are dominated by $2C_O$-Zn_i (1.81 eV), $3C_O$ (1.87 eV), and $2C_O$-V_O-Zn_i (1.90 eV), with Type 2B additionally having a sizeable population of C_O-V_O similarly to Type 1B.

2 Methods

2.1 Sample synthesis

The NWs studied in this work were grown via chemical vapor deposition (CVD). A precursor mixture of ZnO (Sigma Aldrich 255750, 99.99% purity) and graphite (Sigma Aldrich 282863,

< 20 μm, synthetic) powder in ZnO:C mass ratio of 1:1 (for Type 1A and Type 1B NWs with predominantly green fluorescence) or 1:3 (for Type 2A and Type 2B NWs with predominantly red fluorescence) was grounded and thoroughly mixed in an agate mortar and pestle for 45 min. 0.4 g (measured with Mettler Toledo ME204 analytical balance) of the mixture was then transferred to the end of a quartz tube with inner diameter of 16.0 mm and outer diameter of 19.2 mm. 2 cm long silicon substrates pre-deposited with polycrystalline undoped ZnO seed layer through 100 W radio-frequency (RF) sputtering were placed in the quartz tube 15 cm upstream of the precursor powder. The quartz tube was placed in a Carbolite horizontal tube furnace such that the powder resided at the centre of the furnace. The powder was heated with a ramping rate of 40 °C/min and held at 910 °C for 5 h. The reaction took place in the presence of carrier gas comprising 0.5% oxygen and 99.5% argon with a flow rate of 199 sccm (monitored by MKS Type 247 four channel flow controller power supply and readout) under a working pressure of 1.8 mbar (monitored by Edwards active digital pressure controller standard version). The pressure was maintained by an Edwards RV5 rotary vane pump. After the 5-h heating cycle was completed, the sample was left to cool overnight before being extracted from the furnace.

2.2 Irradiation methodology

5–20 keV electron energy irradiation was carried out in a JEOL JSM 6700F field emission scanning electron microscopy (SEM). Unless otherwise specified, irradiation was generally carried out at 450,000 times of magnification (corresponding to a viewport area of approximately 190 nm by 270 nm or 50,900 nm^2), 10 μA of emission current, 60 pA of probe current (corresponding to 3.75×10^8 $e^- \cdot s^{-1}$), 0.2086 ms of horizontal scanning time, and 0.28 s of vertical scanning time. The start of irradiation durations was taken as the moment magnification was increased to 450,000 times. The end of irradiation was taken as the moment magnification was decreased. When commencing and halting irradiation, effort was made to increase and decrease the magnification in 1 s or less.

2.3 Scanning electron microscopy and energy dispersive X-ray spectroscopy

SEM images were captured in the abovementioned JEOL JSM 6700F SEM with an emission current of 10 μA. Images captured in secondary electron imaging mode were captured at a working distance of 8 mm, with an accelerating voltage of 5 kV. Images captured concurrently with energy dispersive X-ray (EDX) measurements were captured with a working distance of 15 mm and an accelerating voltage of 5 kV. EDX measurements were captured with an Oxford Instruments X-MaxN 150 detector coupled with the SEM at a working distance of 15 mm. Unless otherwise specified, EDX maps were captured over one integration with pixel dwell time of 2 ms. The exposure of elemental map images was uniformly increased by the same factor in post-processing for visual clarity.

2.4 Optical microscopy (OM) and fluorescence microscopy (FM)

Optical bright field (OM) and fluorescence micrographs (FM) were captured in an Olympus BX-53 fluorescence microscope coupled with a halogen lamp and an Olympus U-HGLGPS (130 W) mercury burner lamp. Broadband ultraviolet, blue, green, and yellow excitation were selected using Olympus U-MWU2, U-MWB2, UMWG2, and U-MWG2 filter cubes, respectively. The filter cubes were low pass filters for emission signals, i.e., they removed the excitation wavelength and shorter wavelengths from the sample signal. Images were captured through an Olympus MPLFLN100 (100× magnification, numerical aperture of 0.9) objective lens. Polarized micrographs were captured by inserting a rotatable Olympus U-AN360P polarizer between the objective lens and camera.

2.5 Photoluminescence spectroscopy

PL spectra were measured with a Renishaw inVia micro-Raman spectroscope with 1800 lines/mm grating. Sample emissions were captured through a Leica DMLM microscope with Thorlabs LMU-40×-NUV objective lens at 40× magnification. The excitation wavelength was 325 nm produced by a helium-cadmium laser. A notch filter was used to remove the excitation wavelength from the signal.

2.6 Atomic force microscopy (AFM)

AFM measurements were captured in a Bruker Dimension Icon AFM with TESPA-V2 tip in tapping mode using a scan rate of 0.1 Hz and 512 samples per line.

2.7 Transmission electron microscopy (TEM)

TEM images were captured in a JEOL JEM 3010 TEM and a JEOL JEM 2010F field emission TEM. Image capture exposure time was 0.3 s in the 3010 and 0.2 s in the 2010F.

2.8 X-ray photoelectron spectroscopy

XPS measurements were conducted in a Kratos AXIS Supra+. Narrow scans were performed for C 1s, O 1s, and Zn 2p. Peak fitting was performed in KherveFitting Ver. 1.4 code [23]. Atomic sensitivity factors (ASF) were accounted for by selecting the "KratosF1s-Al1486" configuration for instrument setting. Tanuma, Penn, and Powell (TPP-2M) formula was chosen for the energy compensation factor (ECF) profile to account for inelastic mean free path. Voigt subpeaks with 20:80 Lorentzian/Gaussian contribution were fit to the narrow scans. The full width at half maximum (FWHM) for the subpeaks of each element was constrained to approximately the same value as the FWHM for the largest component subpeak. Additionally, for Zn 2p, a constrained doublet was fit to both the Zn $2p_{3/2}$ and Zn $2p_{1/2}$ simultaneously.

2.9 Monte Carlo simulations

Electron–matter interaction Monte Carlo simulations were conducted in Casino V3.3.0.4 [24]. ZnO-C nanowires were modelled as cylinders with 64 circumferential divisions, a length of 10 μm, and diameters varying from 100 to 400 nm in intervals of 50 nm. The density was assumed to be approximately the same as bulk ZnO and set to 5.6 g/cm^3 [25]. The stoichiometry of Zn:O:C was set to 0.5:0.45:0.05. The proportion of oxygen to zinc was lowered to account for oxygen vacancies being energetically favorable to form in ZnO [6] and general agreement that oxygen vacancies were frequently present in experimental samples [1, 4, 26]. For secondary electron (SE) simulations, plasmon energy was set to 18.8 eV [27, 28] and work function was set to 4.7 eV [29] . The electron beam was modelled as a cylindrical spot irradiation with a diameter of 10 nm and a spacing of 0.05 nm between electrons. Electron energy was varied between 1 and 50 keV in steps

of 1 keV. 10,000 electrons were simulated in each run and 5 runs were conducted to obtain an average for the data. Electron trajectories were considered halted when the electron energy decreased to less than 50 eV.

3 Results

Localized electron irradiation was carried out by irradiating ZnO-C NWs and NBs with 5–20 keV electrons in a 9.63×10^{-5} Pa vacuum at 450,000 times magnification. This magnification corresponded to a 190 nm by 270 nm viewport. During irradiation, the SEM was operated in coarse scan mode such that the electron emission was scanned across the viewport with a horizontal scanning time of 0.2086 ms and a vertical scanning time of 0.28 s. More detailed irradiation parameters are provided in Section 2. While stray electron irradiation cannot be discounted during image acquisition at low magnification, the effects on the NWs due to electron dose applied at low magnification were considered negligible compared to the effects caused by high magnification irradiation when the dose density was orders of magnitude higher.

3.1 Optical modification

High magnification LEE irradiation produced localized sub-micron changes in the defect fluorescence of ZnO-C NWs. Figure 1 shows optical bright field micrographs (OM) and ultraviolet-excited (UV) fluorescence micrographs (FM) that display the variety of changes in visible band defect fluorescence in the four types of NWs. Figure 1(a) shows OM and UV FM images of a Type 1A NW before and after irradiation by 5 keV electrons for 1 min. The OM images showed no apparent changes. However, under UV excitation, the defect fluorescence exhibited localized quenched intensity at the irradiated location. It should be noted that the segment of the NW that exhibited quenched intensity was not ablated by the electron beam and was visible in the OM image. Additionally, the fluorescence quenching was heterogeneous, leaving behind a spotty pattern of fluorescence rather than a continuous band of darkness.

Figure 1(b) shows UV FM images of a Type 2A NW before and after irradiation with the same conditions as that used in Fig. 1(a). In contrast to the behavior shown by the Type 1A NW, the Type 2A NW exhibited enhanced fluorescence at the irradiated spot.

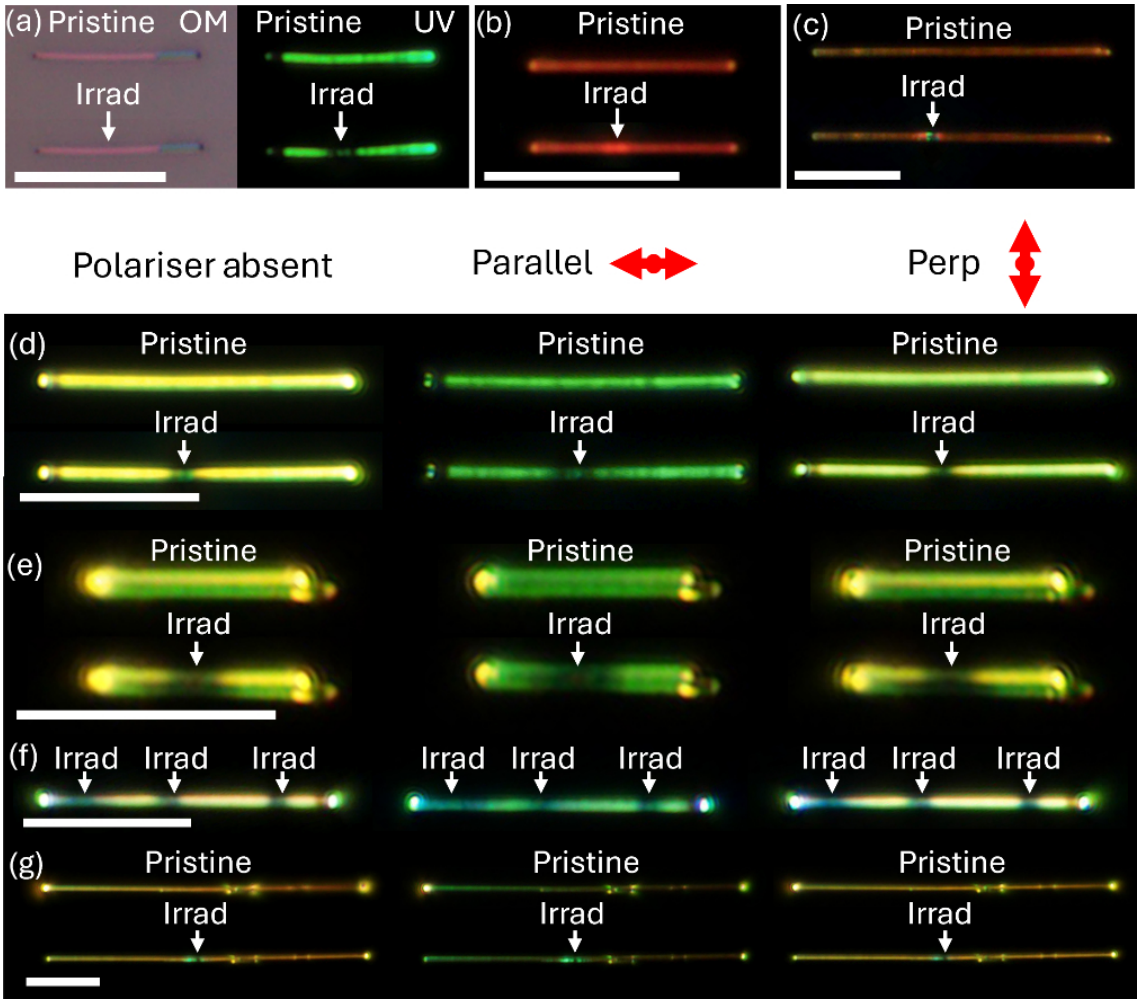

Figure 1 Localized fluorescence modification via high magnification LEE irradiation. (a) Optical bright field and FM of Type 1A NW before and after irradiation. UV: ultraviolet-excited fluorescence. ((b) and (c)) UV FM images of Type 2A NWs before and after irradiation. ((d)–(g)) Polarized FM images of ((d)–(f)) Type 1B and (g) Type 2B NWs with polarized emission components before and after irradiation. White arrows indicate irradiation locations. Red double-headed arrows indicate analyzer transmission axis orientation with respect to the images. Irradiation conditions (electron energy and irradiation duration): ((a) and (b)) 5 keV and 1 min, (c) 5 keV and 2 min, (d) 5 keV and 20 min, (e) 20 keV and 2 min, (f) 5 keV and 2 min, and (g) 5 keV and 10 min. Probe current is the same for all NWs at 60 pA. Scale bars: 10 μm. NW diameters: (a) 440, (b) 330, (c) 510, (d) 360, (e) 640 (combined), (f) 430, and (g) 510 nm.

Similar to the Type 1A NW, the spatial extent of the modified fluorescence extended beyond the viewport of the SEM during irradiation, likely indicating electron flow lengthwise along the NW. Figure 1(c) shows UV FM images of a second Type 2A NW subject to localized irradiation. Like the NW in Fig. 1(b), fluorescence intensity was enhanced by electron irradiation but with a slight dip in intensity at the irradiated spot. Additionally, the location that was directly irradiated changed color from red to green. Aside from the difference in probe current, the differences in behavior could be attributed to unavoidable differences between NWs due to the stochastic nature of nanostructure growth. Comparing the pristine states of both Type 2A NWs, it was observed that the NW in Fig. 1(c) displayed browner and more heterogeneous defect fluorescence, with shades of green being visible on the left end of the NW.

Figure 1(d) shows a Type 1B NW with two main defect emission colors. Before discussing the irradiation-induced changes, it is useful to briefly introduce the properties of Type 1B NWs. Type 1B (and Type 2B) NWs are distinguished by the presence of a yellow defect fluorescence of 2.2 eV that is strongly polarized perpendicular to the long axis of the NW. This polarized fluorescence coexists with the underlying defect fluorescence color that is dominant in the samples from which it was fabricated (green fluorescence for Type 1 NWs; red fluorescence for Type 2 NWs). The polarized fluorescence was attributed to a C_O-V_O defect complex [21]. The electron transition responsible for the polarized behavior occurs between neighboring zinc and carbon atoms that lie in a horizontal plane perpendicular to the growth axis of ZnO. A linear polarizer is helpful for visually separating the polarized fluorescence component in Type B NWs. The pristine NW in Fig. 1(d) is now discussed as an example. The leftmost column shows the visible band defect fluorescence when viewed through the fluorescence microscope. The second and third columns show the defect fluorescence when viewed through linear polarizers, with the double-headed red arrows indicating the orientation of the polarizer transmission axis with respect to the fluorescence micrograph. The green emission was unpolarized and was detectable in all polarizer configurations. However, the yellow emission dominated when the polarizer was absent due to its higher intensity than the green emission. The yellow emission also dominated in perpendicular polarizer configuration while being absent in the parallel configuration due to the emission being polarized perpendicular to the NW long axis. In parallel polarizer configuration, the polarized yellow emission intensity was reduced sufficiently for the unpolarized green emission to be visible. A linear polarizer can thus be used to distinguish the effects of electron irradiation on the two types of defect fluorescence.

We now return to discussing the effects of localized electron irradiation of the Type 1B NW in Fig. 1(d). Prior to irradiation, the NW displayed uniform fluorescence in all polarizer configurations. After the centre of the NW was irradiated by 5 keV electrons for 20 min, the green emission was visible at the irradiated spot when the polarizer was absent (leftmost column of Fig. 1(d)), indicating that the yellow emission was more strongly quenched than the green emission. Additionally, by comparing the images obtained under parallel (middle column of Fig. 1(d)) and perpendicular (rightmost column of Fig. 1(d)) polarizer configurations, it was observed that the quenching of the yellow emission was more localized than the green emission. A more direct comparison of quenching extent can be seen in Fig. 1(e), which shows a twinned NW with yellow and green emission segments running parallel before and after it was subject to localized 20 keV electron irradiation for 2 min. When the polarizer was absent and under perpendicular polarizer configuration, the half with green fluorescence showed a longer quenched segment than the half with yellow fluorescence. Under parallel polarizer configuration, the green fluorescence for both halves showed approximately equal quenching lengths.

Figure 1(f) shows an example of how localized and defect-specific quenching could be used to engineer axial heterostructures along the NW that display different fluorescence patterns. Localized irradiation in three distinct spots of a NW with initially uniform fluorescence produced a NW with alternating segments of green and yellow fluorescence, with the segments also possessing alternating polarization properties. This NW demonstrates how binary patterns can be encoded on Type 1B NWs. These patterns are invisible under optical viewing and can only be detected when the NW is illuminated by ultraviolet light. Additionally, the ability to modify the emission polarization with spatial selectivity further enhances the flexibility with which these NWs can be applied for polarimetry.

Figure 1(g) shows UV-excited polarized FM images of a Type 2B NW before and after localized irradiation. Similar to the Type 2A NW in Fig. 1(c), fluorescence intensity enhancement was observed in the vicinity of the irradiated spot while intensity decreased at the spot that was directly irradiated. Comparing the three polarizer configurations, it was concluded that electron irradiation enhanced the unpolarized emission component while quenching the perpendicularly polarized component. Additionally, color conversion to green was observed near the irradiated spot under unpolarized and perpendicularly polarized configurations. Based on the observations from the Type 2A NW in Fig. 1(c), this was likely a similar color conversion of the unpolarized emission component. While the Type 2B NW in Fig. 1(g) appeared homogeneous when viewed without polarizer (leftmost column), the parallel polarized images (middle column) revealed more heterogeneity in the unpolarized emission compared to the NWs in Figs. 1(b) and 1(c). The unpolarized emission showed a gradation from green on the left to reddish-brown on the right. The reddish brown color observed without polarizer was thus contributed in larger part by the perpendicular polarized emission (rightmost column). Examining the parallel polarized images (middle column), the centre of the NW showed a mix of green and red fluorescence prior to irradiation. After electron irradiation, the mix of green and red fluorescence was completely converted to green and fluorescence intensity was enhanced. This matches the behavior shown in Figs. 1(b) and 1(c). Under perpendicular polarizer configuration (rightmost column), the polarized yellow emission was quenched by irradiation, allowing the enhanced unpolarized green-converted emission to dominate.

The dependence of irradiation-induced changes on electron energy, electron dose, irradiation duration, emission current, probe current, and magnification was investigated. Of these parameters, varying electron dose and electron dose rate (probe current) showed the most pronounced changes in optical modifications. Morphological modifications were more influenced by irradiation duration and electron energy.

Figure 2 shows results of further investigation on Type 1A NWs. Figure 2(a) shows UV FM and OM images of a Type 1A NW that was repeatedly irradiated by 5 keV electrons in intervals of 5 s at the

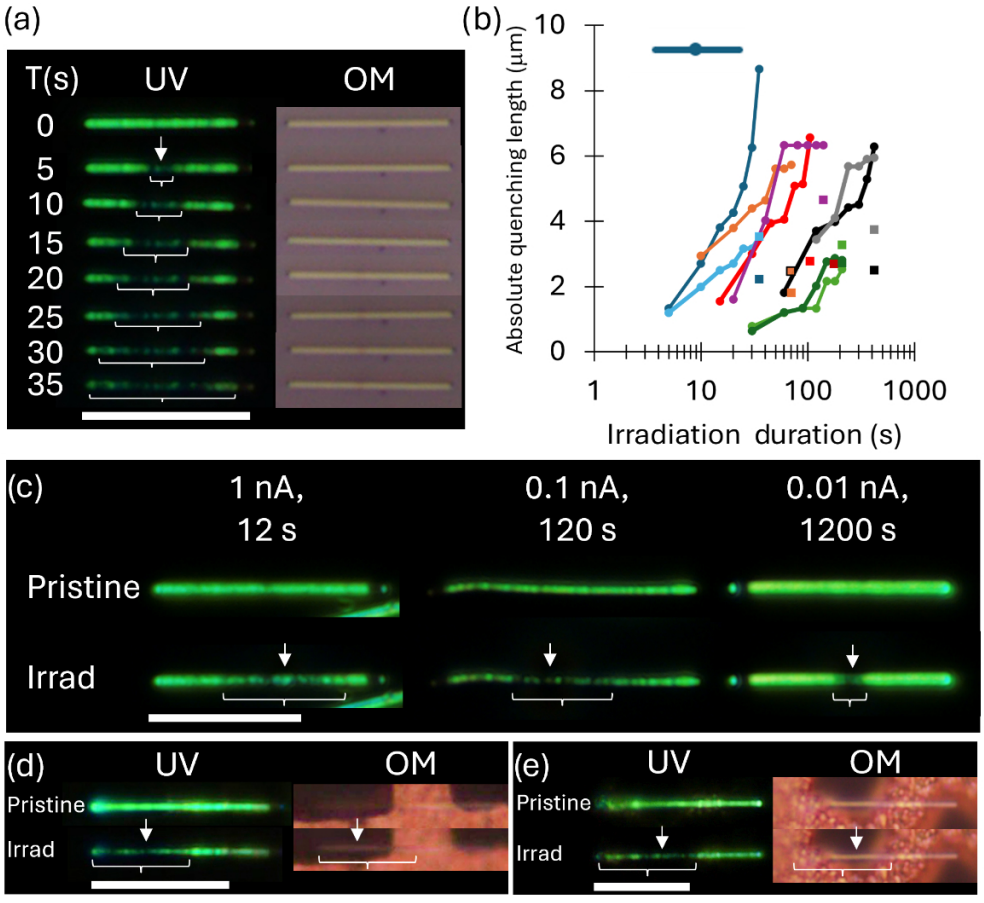

Figure 2 High magnification LEE irradiation of Type 1A NWs. White arrows indicate irradiation locations, and white curly braces indicate the length that was considered quenched. (a) Timelapse UV-excited FM images (UV) and optical bright field images (OM) of a NW supported by silicon substrate repeatedly subject to intervals of irradiation of 5 s by 5 keV electrons. The NW was removed from the SEM chamber after each interval of 5 s for imaging. Irradiation was always aimed at the same spot on the NW. (b) Linear-log plot of length of quenched fluorescence against irradiation duration for the NW in (a) and 19 other NWs. Different NWs were irradiated with different quanta of durations. Round points with lines correspond to NWs that were repeatedly irradiated and then removed from the SEM for imaging. Isolated square points correspond to NWs that were irradiated only for one session before imaging. FM and OM images for the 19 other NWs are provided in Fig. S1 in the ESM. (c) Three separate NWs supported by silicon substrate subject to irradiation by varying combinations of probe current and irradiation duration such that the total electron dose was the same for all three. ((d) and (e)) NWs suspended on copper TEM grid. The NWs were irradiated at locations hanging over the holes in the copper grid by 5 keV electrons for (d) 15 s and (e) 10 min. NW diameters: (a) 370 nm, (c) (left to right) 410, 200, and 320 nm, (d) 400 nm, and (e) 570 nm. Scale bars: 10 μm.

same part of the NW (marked by the white arrow). After each interval of irradiation, the NW was removed from the SEM for imaging. The FM images showed that the length of quenched fluorescence increased with cumulative irradiations. The OM images showed a slight darkening of the NW where irradiation was concentrated. This darkening was due to a gradual build-up of carbon due to EBID which will be discussed further in the later section.

The absolute quenching length was measured by comparing the fluorescence brightness against the pristine state of the NW. Parts that were darkened or converted into "beads" of heterogeneous fluorescence were considered quenched. The absolute quenching length was plotted against irradiation duration in Fig. 2(b). 19 other NWs were investigated in a similar way with different irradiation duration intervals. Round points connected by solid lines correspond to NWs treated similarly to the NW in Fig. 2(a), where the NW was repeatedly irradiated and removed from the SEM for imaging. To investigate the influence of repeated removal from the SEM chamber, single interval irradiation tests were also performed. The isolated square points correspond to NWs that were irradiated for equivalent durations to the cumulative durations used to treat the NWs that were repeatedly removed. For example, the NW in Fig. 2(a) was irradiated for a total of 7 intervals of 5 s. Equivalently, another NW was irradiated for 35 s in a single interval and the quenching length was measured. The rounded and square points in Fig. 2(b) were color-coded such that NWs treated with equivalent total durations have the same color. The OM and FM images of all 20 NWs and an additional plot of fractional quenching length against irradiation duration are provided in Fig. S1 in the Electronic Supplementary Material (ESM).

Generally, quenching length increased monotonically with irradiation duration for both types of treatment. For two of the NWs, the plateauing of quenching length was due to the entire NW having become quenched. The increase in quenching length with electron dose was due to electrons flowing lengthwise along the NW and electrons discharging into the underlying silicon substrate and spreading outwards. Figure S2 in the ESM provides evidence for both these effects. Figure S2(a) in the ESM shows an SEM image of the substrate under an irradiated NW that was subsequently removed from the substrate. The dark patches on the substrate

indicate areas where electrons discharged into the substrate during irradiation. The presence of dark patches on the opposite side of the irradiated spot implied that electrons flowed lengthwise along the NW and discharged into the substrate on the opposite side. Figure S2(b) in the ESM shows that proximate NWs that were not in physical contact still displayed fluorescence quenching due to electrons flowing in the substrate under the NWs.

NWs irradiated in a single interval generally showed shorter quenching length than NWs that were irradiated for the equivalent cumulative duration over multiple intervals. There are two possible explanations for this. Firstly, while effort was made to rapidly increase and decrease the SEM magnifications at the start and end of irradiation, stray irradiation during sample acquisition at low magnifications would have delivered an unavoidable extra dose of electrons. There would thus be an underestimation in the stated irradiation duration. To minimize the percentage error that this would cause, longer irradiation intervals were also used (seven intervals of 1-min durations). In these longer interval tests, a similar trend was still observed where NWs that were irradiated in multiple intervals and repeatedly removed from the SEM displayed close to double the quenching length compared to NWs that were irradiated in a single interval. The electron dose underestimation thus cannot be the full explanation.

A second possible contributing effect is the discharging of the NW and underlying silicon substrate by ambient moisture when the samples were removed from the SEM chamber. As will be explained in greater detail later, the radius over which electrons discharge into the substrate is based on the amount of substrate charging. If electrons can be discharged efficiently, they would travel straight down through the substrate to the metallic sample holder. However, if discharging is inefficient compared to rate of incoming electrons, electron pileup would occur, forcing electrons to spread out over the substrate surface so that they can discharge into the substrate over a larger cross-sectional area. The size of the electron pileup depends on the electron dose rate (probe current), electron dose (controlled by irradiation duration), and the conductivity of the substrate bulk and surface. The following mechanism is thus proposed. When electron pileup occurs during electron irradiation, the surface oxide layer within the electron pileup radius is chemically reduced by the abundance of electrons. This improves the surface conductivity within the electron pileup radius while the bulk conductivity remains largely unchanged, leading to a larger electron pileup radius. While the pileup radius can increase with electron dose, the equilibrium size of the pileup radius generally depends on the initial conditions of the substrate upon irradiation. Each time the sample was removed from the SEM chamber, any excess charges would be discharged by ambient moisture, removing the electron pileup. However, the silicon surface is unlikely to re-oxidize as quickly as the electron discharge, meaning that the initial conditions for subsequent irradiations tend towards larger surface conductivity to bulk conductivity ratios. Thus, larger electron pileup radii occur in subsequent irradiations, resulting in an increased length of NW exposed to electron interaction and hence increased quenching length.

Figure 2(c) shows the UV FM images of three separate Type 1A NWs supported on silicon substrate irradiated by different combinations of probe current and irradiation duration such that the total electron dose delivered to each NW was the same. The results showed that quenching length was longer for higher probe current. This could be understood from the same mechanism discussed in the paragraph above. Higher probe currents caused a larger electron pileup radius. Thus, longer segments of the NW would interact with electrons and experience fluorescence quenching.

Figures 2(d) and 2(e) show UV FM and OM images of two separate NWs suspended on copper TEM grids. The parts of the NWs hanging over a hole in the grid were irradiated with 5 keV electrons and with the same probe current for 15 s and 10 min, respectively. In both cases, the NW segments hanging over the hole displayed fluorescence quenching while the segments in contact with the copper grid showed minimal quenching. Moreover, compared to NWs supported on silicon substrate where electrons could discharge directly into the substrate under the NW, majority of the observations showed that longer fluorescence quenching lengths were observed at much lower irradiation durations for NWs supported on copper grids, as Fig. 2(d) demonstrates. These observations can be understood as follows. In the absence of an underlying substrate, the electrons that enter the NW during irradiation must discharge lengthwise through the NW. When the electrons reach the point of electrical contact with the copper grid, they enter the copper grid and leave the rest of the NW untouched. This explains why only the parts above the holes displayed fluorescence quenching.

Figure 3 shows results of further investigation on Type 2A NWs. In contrast with Type 1A NWs, fluorescence intensity was enhanced (at low doses) by electron irradiation rather than quenched and the magnitude of modification was not as drastic. Generally, the dependence on irradiation duration and probe current was also not as pronounced. These observations might indicate that Type 2 NWs are more robust against electron modification. Alternatively, since Type 2 NWs are associated with higher carbon content, defect species with elevated carbon content might also hinder the lengthwise flow of electrons in the NW as the presence of carbon atoms in the ZnO crystal structure acts as scattering centres.

Figure 3(a) shows three separate NWs irradiated by 5 keV electrons at the same probe current for varying irradiation durations. While all three NWs displayed localized fluorescence enhancement in the vicinity of the irradiated spot, the NW irradiated for the longest duration also showed a dip in intensity at the location that was directly irradiated. In contrast to Type 1A NWs, the quenching was homogeneous rather than leaving behind beads of fluorescence. Figure 3(b) shows two NWs irradiated by different combinations of probe current and irradiation duration such that the total dose delivered to both NWs was the same. While both NWs showed fluorescence enhancement, the NW exposed to higher probe current showed enhancement over a longer length, most likely due to the increased electron pileup radius caused by a higher probe current. The NW exposed to higher probe current also showed a dip in intensity at the location that was directly irradiated.

Figure 3(c) shows a Type 2A NW irradiated at multiple spots along the NW. From left to right, the probe current was increased while keeping the irradiation duration the same at 5 min. The OM images showed no discernible changes in the NW after irradiation save for a darkening of the substrate under the NW due to a combination of surface oxide interaction with electrons and EBID of carbon. Under UV excitation, the left side of the NW which was exposed to lower probe currents showed fluorescence enhancement with dips in intensity at the spots that were directly irradiated. The

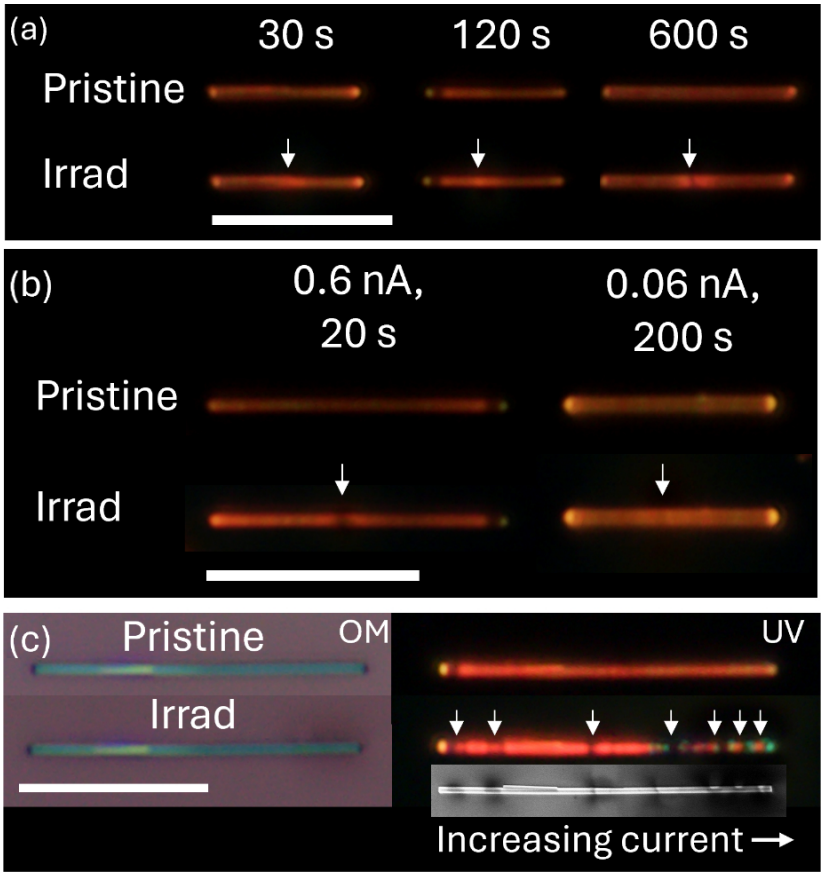

Figure 3 High magnification LEE irradiation of Type 2A NWs. White arrows indicate irradiation locations. (a) UV-excited FM images of three separate NWs irradiated by 5 keV electrons with a probe current of 60 pA for varying durations. (b) UV-excited FM images of two separate NWs irradiated by 5 keV electrons for varying combinations of probe current and irradiation duration such that the total electron dose was the same for both. (c) Optical bright field images (OM) and UV-excited FM images (UV) of a NW irradiated by 5 keV electrons at seven spots along the NW for 5 min each with increasing probe current from left to right: 6 pA, 10 pA, 60 pA, 0.1 nA, 0.6 nA, 1 nA, and 3 nA. The inset SEM image was captured immediately after the seven irradiations were completed. NW diameters (left to right): (a) 350, 270, and 480 nm, (b) 460 and 860 nm, and (c) 540 nm. Scale bars: 10 μm.

dips in intensity became more prominent with increasing probe current, until the fourth irradiated spot (with probe current of 0.1 nA) where fluorescence intensity was heavily quenched. Additionally, the parts of the NW exposed to higher probe currents displayed localized color conversion from red to green. The inset SEM image was captured immediately after the irradiations were completed and was used to pinpoint the irradiated spots. The darkened patches indicate charging effects and were used to visualize electron trajectory. As will be discussed further in the section on EBID, the darkened parts of the NW on the three leftmost irradiated spots indicated EBID of carbon. The brightened patches on the four rightmost spots indicated EBIE associated with higher probe currents. The brightened appearance of the NW under SEM imaging was interpreted to be due to increased secondary electron yield from the ZnO-C upon etching of surface contamination. Closer inspection and cross referencing with the SEM image revealed that the color conversions lay immediately next to the irradiated spots while the spots that were directly irradiated exhibited quenched fluorescence. As will be discussed later, the areas immediately next to parts of the NW that underwent EBIE were associated with elevated surface carbon.

3.2 Morphological modifications

While short duration irradiation was sufficient to produce optical changes, additional morphological changes were observed with longer irradiations at high magnification. Under OM imaging, this typically manifested as a gradual formation of optically dark material on the NW at the irradiated spot. Morphological changes were not apparent at lower magnifications within the irradiation durations used in this work. From this point, investigations of morphological modifications will be concentrated on Type 1A NWs and NBs.

To more systematically investigate the dependence of the outgrowth size and shape on electron irradiation parameters, EBID was conducted on NBs. NBs provided a flatter top surface than NWs, which enabled a more consistent comparison between outgrowths. Figure 4 summarizes the main properties of outgrowth formation. Additional characterization results are provided in the ESM.

Figure 4(a) shows the AFM height images and phase images of a Type 1A NB before and after irradiation by 5 keV electrons with a probe current of 60 pA. Figure 4(b) shows a three-dimensional (3D) height profile image of the NB after irradiation. Each box on the nanobelt corresponded to a region of outgrowth induced by one continuous interval of irradiation. Figure 4(c) summarizes how the height of the NB surface varied with electron dose after subtracting the background slope of the substrate. The height profile was measured along the red dashed line in Fig. 4(a) and the data points

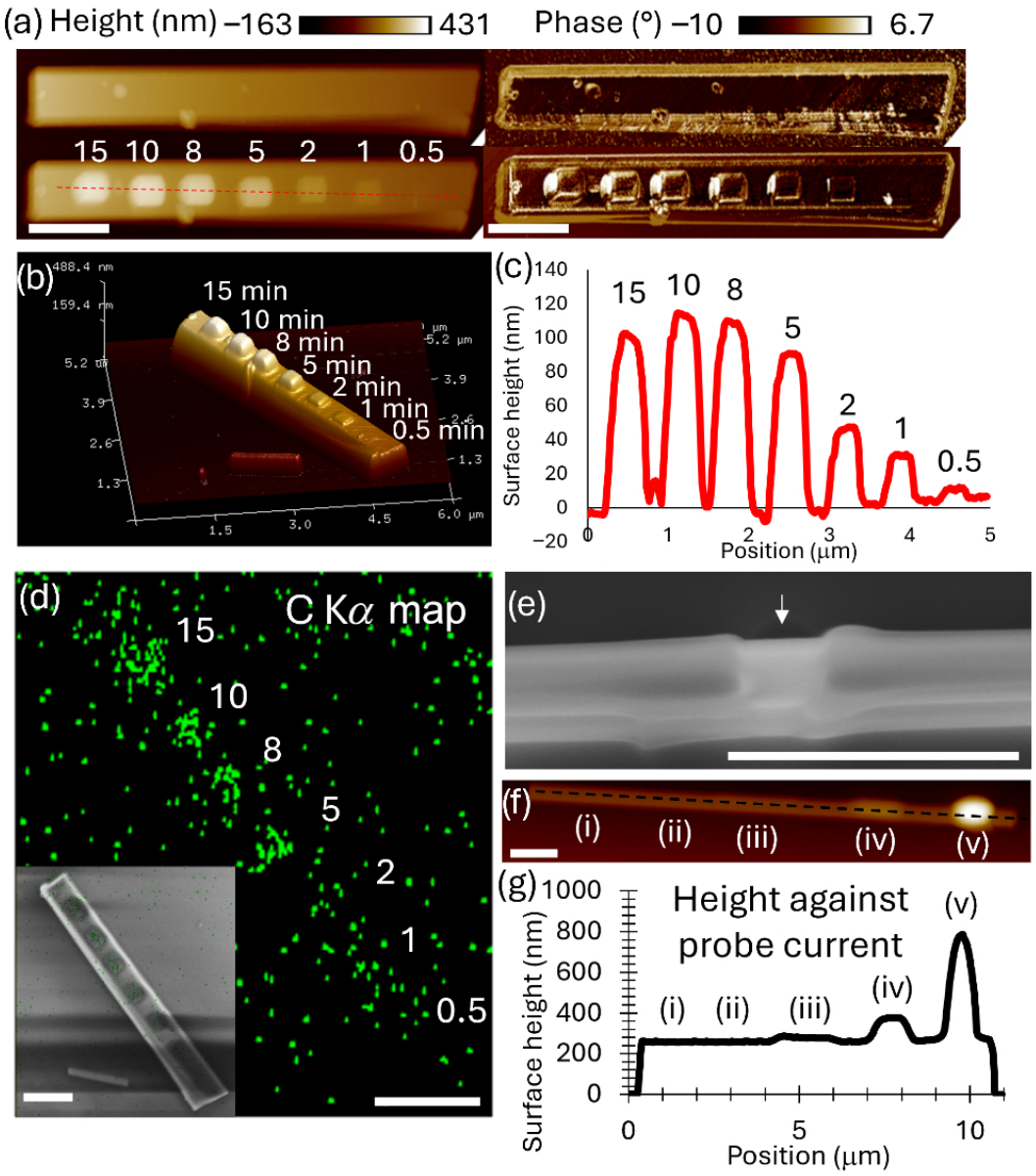

Figure 4 EBID of carbon on Type 1A NBs and NWs. (a) AFM height profile and corresponding phase images of a Type 1A NB before and after irradiation by 5 keV electrons with a probe current of 60 pA for varying durations. The labelled numbers indicate irradiation duration in minutes. (b) 3D height profile image. (c) Line-trace profile along the red dashed line in (a). Flat data points between outgrowths were truncated. The labelled numbers indicate irradiation duration in minutes. (d) EDX carbon elemental map of the NB in (a). Inset: SEM image of the EDX scan area. (e) SEM image of separate NW irradiated by 5 keV electrons with a probe current of 600 pA for 30 min. White arrow indicates irradiated location. (f) AFM height profile image of a second NB irradiated at five locations with varying combinations of probe current and irradiation duration such that the electron dose was the same. Irradiation parameters (probe current and irradiation duration) from left to right: (i) 1 nA and 60 s, (ii) 0.6 nA and 100 s, (iii) 0.1 nA and 600 s, (iv) 60 pA and 1000 s, and (v) 10 pA and 6000 s. (g) Line-trace height profile along the black dashed line in (f). Scale bars: 1 μm.

between the outgrowths were truncated for brevity. Outgrowth height increased with irradiation duration, plateauing at around 112 nm after 10 min of irradiation. A slight decrease in outgrowth height was observed for 15 min of irradiation, but this was likely due to unavoidable inhomogeneities along the nanobelt. Figure 4(d) shows the EDX carbon map for the nanobelt shown in Fig. 4(a). Clusters of elevated carbon concentration were observed in the irradiated regions, with higher electron doses corresponding to higher carbon concentration. The EDX map corroborated the interpretation that the outgrowths were formed from the EBID of carbon.

Figure 4(e) shows a different twinned NW irradiated with higher probe current (600 pA), resulting in a different morphology of outgrowth. Irradiation was concentrated on the rectangle in the centre of the NW. Due to the elevated probe current, EBIE dominated over EBID, causing the irradiated location to be reduced in thickness. However, inflow of carbon due to the surface carbon gradient set up by electron irradiation still caused carbon deposits to form adjacent to the irradiated area, causing an increase in thickness surrounding the irradiated area. This mechanism and the dependence of EBID rate on probe current are well-established in Refs. [30–33]. A similar morphology of elevated outer ridges and

depressed height in the irradiated area has in fact been experimentally observed in EBID studies on planar substrates [30, 32]. Finally, the area affected by EBIE appeared brighter under SEM imaging compared to the pristine parts of the NW, while parts with EBID of carbon appeared darker. This was likely due to differences in work function and secondary electron yield between the etched ZnO-C and deposited amorphous carbon. A timelapse of the formation of Fig. 4(e) is provided in Fig. S3 in the ESM. An additional NW that displayed ridged deposit morphology after irradiation with high probe current is shown in Fig. S4 in the ESM. A more detailed investigation with finer intervals of probe current variation would elucidate the transition between deposition-dominated and etching-dominated outgrowth formation but is the subject of future work.

Figure 4(f) shows the AFM height images of a separate Type 1A NB before and after being irradiated by five combinations of probe current and irradiation duration such that the total electron dose delivered to each location was the same. The irradiation locations are marked with Roman numerals. From left ((i)) to right ((v)), the probe current was decreased, while irradiation duration was increased. The exact irradiation parameters are listed in the figure caption. Figure 4(g) summarizes the variation of height along the black dashed line in Fig. 4(f). Despite the electron dose being kept constant across the irradiated locations, outgrowth height was much taller when irradiation duration was longer, with the outgrowth height at (v) being five times taller than that at (iv). At the tallest, the outgrowth at (v) was three times the thickness of the NB. Similar results for probe current dependence have been observed for EBID experiments on planar substrates in literature. Although the deposition rate should have been expected to decrease from (iv) to (v) based on the probe currents used in this range (60 pA and below) [32], the lower probe current also reduced electron-induced decomposition of the carbon buildup that would have restrained the outgrowth height [30]. It was also possible that system was in the precursor-limited regime where variations in probe current effected little change in deposition rate due to limited precursor availability [30, 34–36]. Meanwhile, decomposition rates still increased with probe current. The outgrowth formation here was thus probably controlled by EBIE rate. Figure S5 in the ESM provides additional AFM phase images and 3D height images related to Figs. 4(f) and 4(g).

Figure 5(a) shows the AFM height profile images and phase images of a ZnO-C NB before and after being irradiated by fixed dose of electrons (15 min of duration) with varied energies, respectively. Figure 5(b) shows a three-dimensional height profile image of the NB after irradiation. Figure 5(c) summarises how the

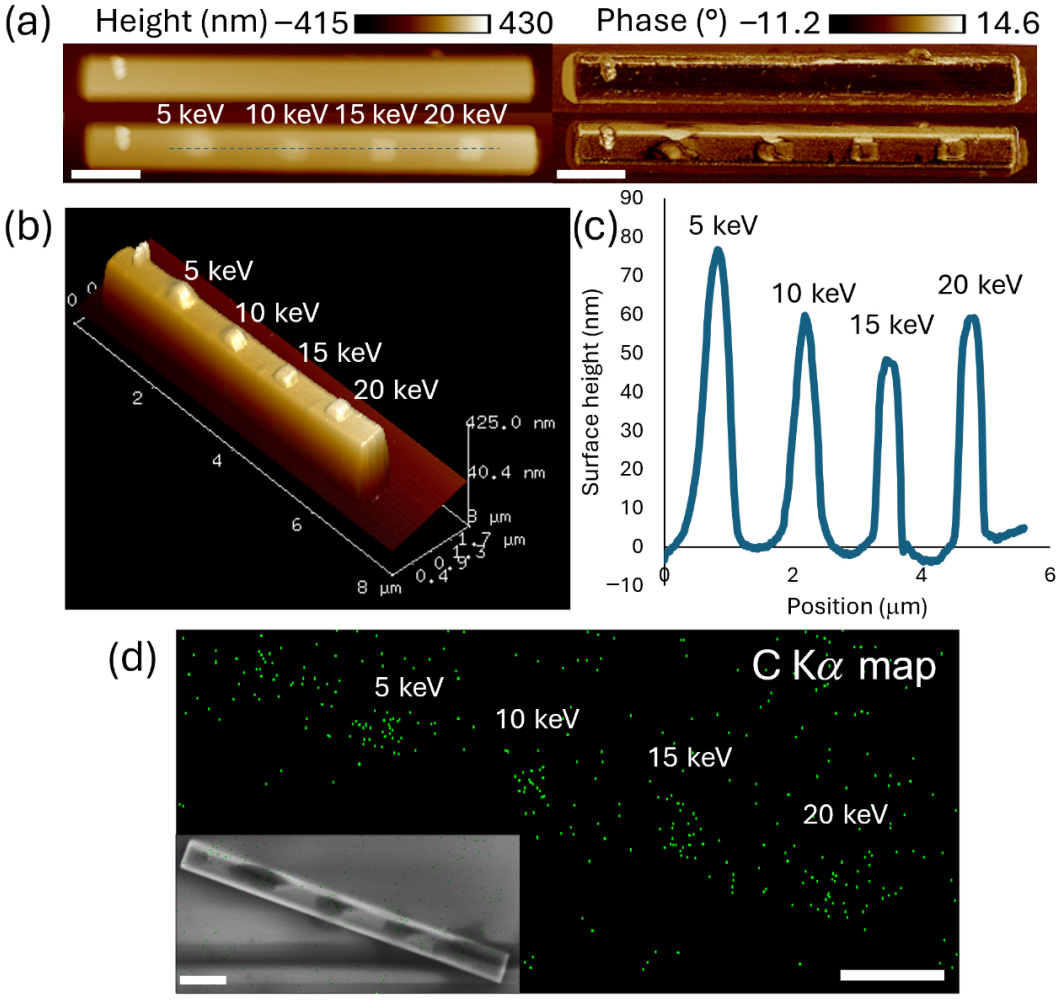

Figure 5 EBID outgrowth height against electron energy. (a) AFM height profile and corresponding phase image of Type 1A ZnO-C NB before and after irradiation. Numbers indicate electron energy. (b) 3D height profile image. (c) Line-trace profile along the dashed line in (a). Flat data points between outgrowths were truncated. (d) EDX carbon elemental maps of the NB in (a). Inset: SEM images of the mapped areas. Scale bars: 1 μm.

height of the NB surface varied with electron dose after subtracting the background slope of the substrate (measured along the blue dashed line in Fig. 5(a) with data points between outgrowths truncated). Outgrowth height generally decreased with increasing electron energy. The increase in height from 15 to 20 keV could likely be attributed to nanobelt inhomogeneities. Additionally, the shape of the outgrowth also varied with electron energy. The lower the energy, the wider the base of the outgrowth and sharper the top. This was attributed to lower energy electrons experiencing more collisions in the NW and depositing their energy over a wider radius, as will be explained in the section on Monte Carlo simulations. Figure 5(d) shows the EDX carbon map for the nanobelt shown in Fig. 5(a). Clusters of elevated carbon concentration were observed in the irradiated region, but a trend against electron energy was not as apparent.

Since EBID in scanning mode produced regular and reproducible rectangles that corresponded with the SEM viewing area, it was possible to perform nanoscale printing. Figure 6(a) shows AFM images of a Type 1A nanobelt before and after the left end of the nanobelt was irradiated with 10 keV electrons in a field emission SEM. The letter "N" was imprinted on the nanobelt by sequentially translating and rotating the viewing area to connect adjacent outgrowths and form lines. While outgrowth primarily occurred in the out-of-plane direction with respect to the substrate, it was also possible to induce outgrowth in the in-plane direction by irradiating the edges of the nanobelt. Figure 6(b) shows a corresponding SEM image of the region after imprinting was completed.

Figure 6(c) shows an enlarged SEM image of the imprinted N overlayed with an EDX carbon elemental map obtained with 5 keV electrons. Figure 6(d) shows the carbon map without the SEM image. Low energy electrons with low penetration were used for the EDX scan to improve the signal from the NW surface and reduce signal from the underlying substrate. Higher concentrations of carbon were observed in the areas with outgrowth, indicating higher degree of carbon incorporation in the outgrowths. The "N" is distinguishable in the carbon map, but not apparent in the zinc or oxygen map, as shown in Figs. 6(e) and 6(f).

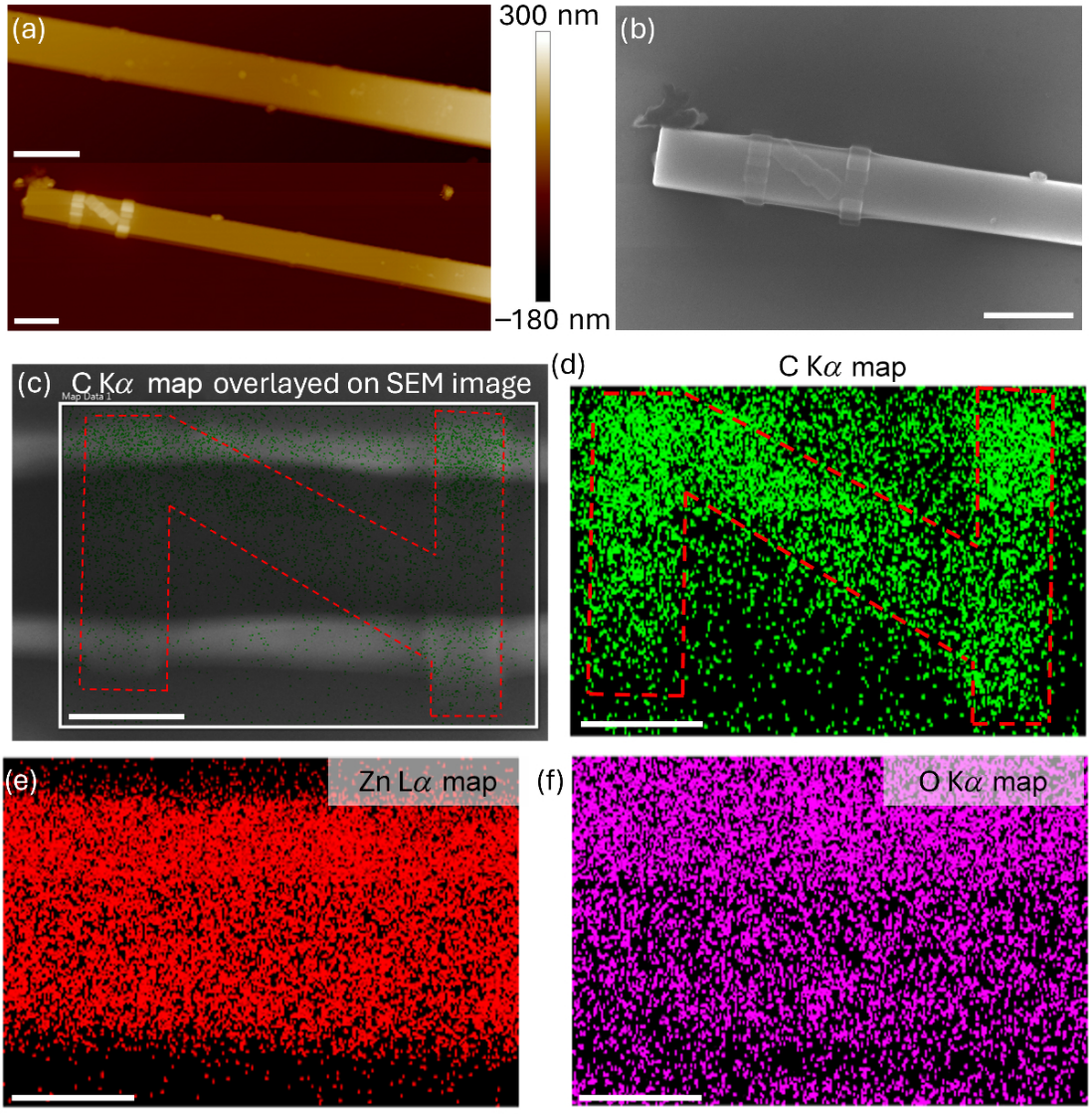

Figure 6 Nanoscale printing via EBID. (a) AFM surface height image of ZnO-C nanobelt before and after "N" is printed on the left side via 10 keV electron irradiation. (b) SEM image of the "N". (c) Magnified SEM image overlayed with EDX carbon elemental map. Red dashed line traces out the "N". (d) EDX carbon elemental map of the white boxed region in (c). Red dashed lines trace out the same "N" as in (c). (e) Zinc and (f) oxygen EDX maps. Scale bars: 1 μm.

3.3 Transmission electron microscopy

During EBID experiments, it was observed that concentrating irradiation close to the side of NWs enabled the formation of EBID outgrowths laterally outwards from the side of the NWs. This enabled the analysis of the outgrowths under TEM. NWs were dry transferred to a copper TEM grid. A suspended segment of a NW was then irradiated with LEE in a field emission SEM before being imaged under TEM.

Figures 7(a)–7(c) show progressively higher magnification TEM images of an EBID outgrowth on a Type 1A NW. The lateral outgrowth could be as thick as 45 nm, which was approximately 22% of the original NW thickness. Figure 7(d) shows the Fast Fourier transform (FFT) of the white dashed-boxed region in Fig. 7(c). Although striated bands were observed in Fig. 5(c), the FFT suggested that the outgrowth was largely amorphous. Figure S6 in the ESM shows TEM images of additional NWs with EBID outgrowths. The outgrowths were also amorphous but with discernible striations in some NWs, such as the diagonal striations in Figs. S6(b)(ii) and S6(b)(iii) in the ESM.

3.4 X-ray photoelectron spectroscopy

To investigate the change in chemical composition of ZnO-C NWs upon LEE irradiation, XPS analysis was conducted on a dense array of Type 1 ZnO-C NWs. Patches of the array were sequentially irradiated under 200,000 times magnification (corresponding to a viewport area of approximately 0.02 μm^2) with 5 keV electrons. After 10 min, the SEM viewport was shifted to irradiate the next patch. Although the irradiated patches were not immediately adjacent to one another, fluorescence imaging of the irradiated array showed that this irradiation protocol resulted in parallel continuous strips of quenched fluorescence due to the dispersal of electrons into parts of the array outside the viewport. The fluorescence quenching indicated successful electron–NW interaction. The total treated area measured approximately 500 μm by 1100 μm. XPS measurements were conducted on four separate irradiated locations and compared to an unirradiated location. Measurements were conducted one month after irradiation to reduce the impact of transient effects like charging. Narrow scans were conducted for Zn 2p, C 1s, and O 1s signals.

Figure 8(a) compares the atomic concentrations of the three narrow scan elements between the unirradiated (labelled "Pristine") and irradiated locations. The LEE irradiated locations displayed higher carbon concentration, lower zinc concentration, and approximately the same oxygen concentration.

Figures 8(b)–8(g) compare the narrow scans of the Zn 2p doublet, C 1s, and O 1s signals between the pristine location and one of the irradiated locations. Figure S7 in the ESM provides a summary of the C 1s and O 1s peak area ratios for the other irradiated locations. The peak fitting procedure is explained in detail in the Methods section.

For Zn $2p_{3/2}$ (Figs. 8(b) and 8(c)), the peak position was observed at an average value of 1021.4 eV, which is 0.7 eV lower than literature values for pure ZnO at 1022.1 eV. The lower binding energy suggests a reduced oxygen concentration surrounding zinc ions, which can be explained by the presence of substitutional

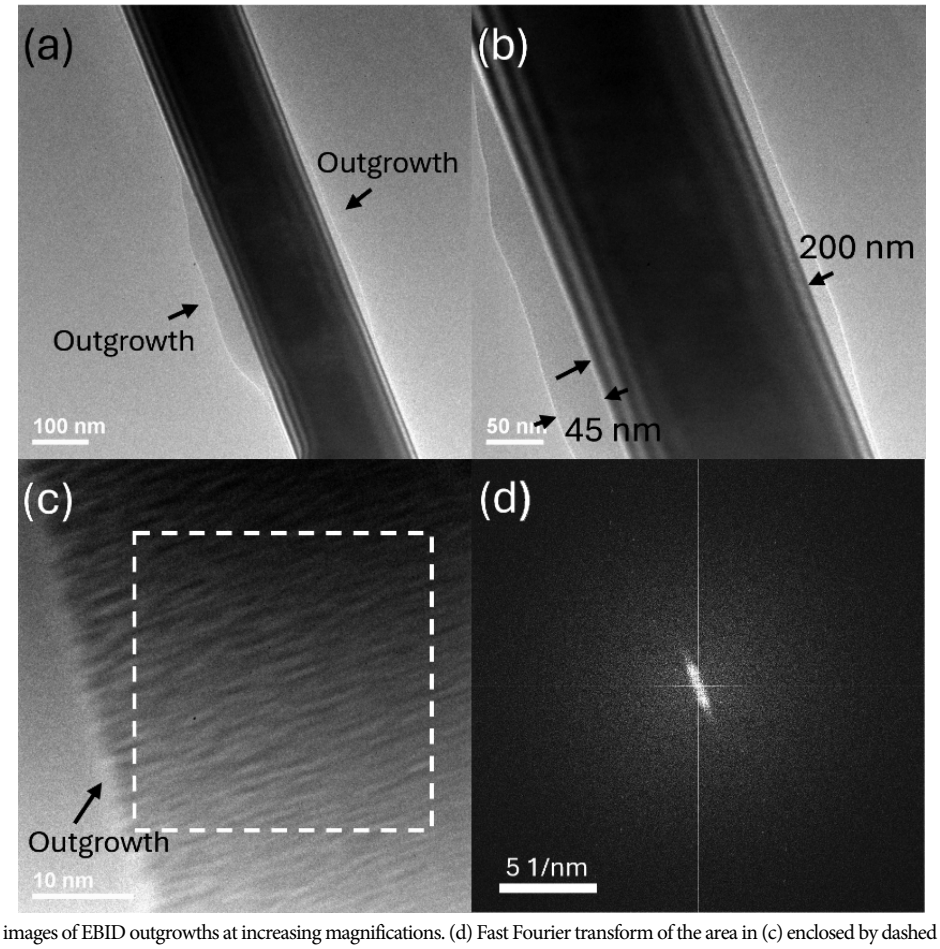

Figure 7 ((a)–(c)) TEM images of EBID outgrowths at increasing magnifications. (d) Fast Fourier transform of the area in (c) enclosed by dashed white box.

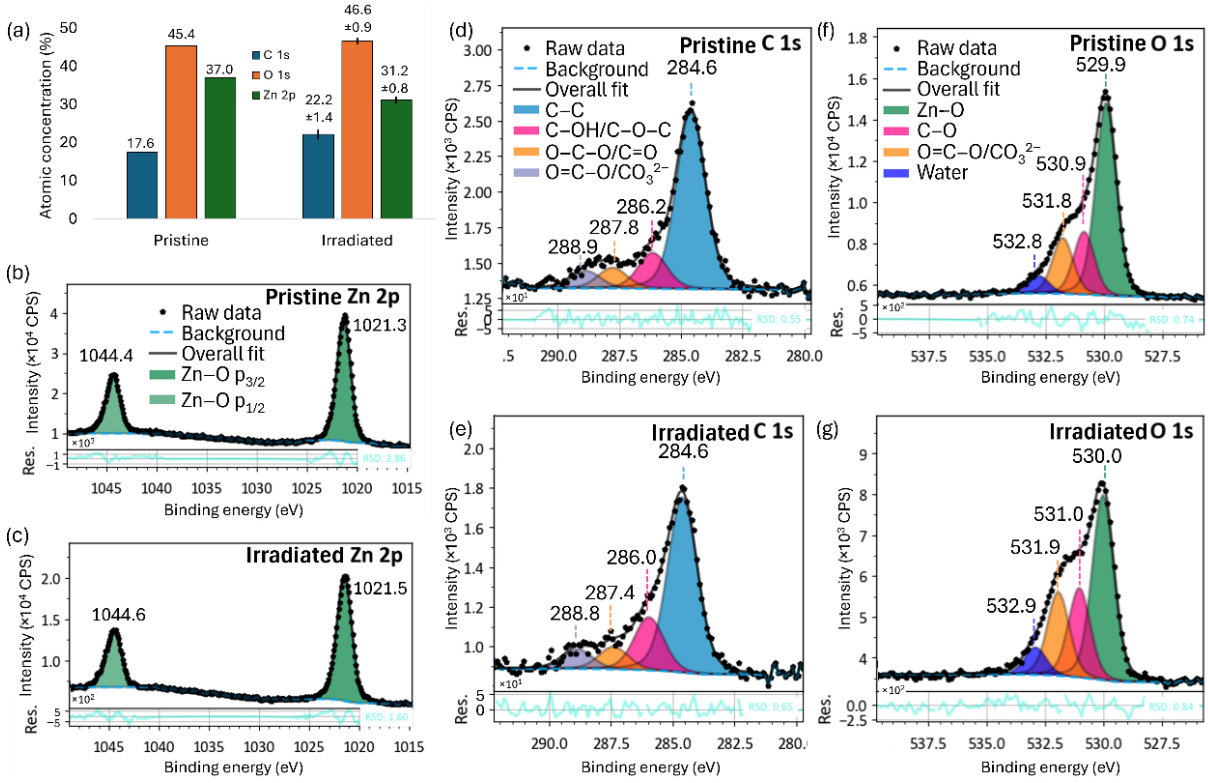

Figure 8 X-ray photoelectron spectroscopy measurements of dense Type 1 ZnO-C NW array sample. (a) Atomic concentration derived from C 1s, O 1s, and Zn 2p signals obtained from one pristine area and four irradiated areas. ((b)–(g)) Narrow scans of ((b) and (c)) Zn 2p, ((d) and (e)) C 1s, and ((f) and (g)) O 1s from ((b), (d), and (f)) pristine and ((c), (e), and (g)) irradiated areas. Labelled numbers indicate binding energy of fitted peaks. The bonds attributed to each peak are indicated in the legends.

carbon dopants. A very slight increase in binding energy (+0.1 eV) was observed after irradiation, which would imply an increase in oxygen concentration, or equivalently, a decrease in zinc concentration. Notably absent was a zinc carbide subpeak which would have appeared at a lower binding energy than the ZnO subpeak.

For C 1s (Figs. 8(d) and 8(e)), the 284.6 eV subpeak was assigned to C–C bonds from adventitious carbon. The remaining subpeaks were analyzed by comparing their area ratios relative to the C–C subpeak. The subpeaks between 286 and 288 eV were attributed to signals from carbon bonded to oxygen in configurations such as C–OH hydroxyl bonds, C–O–C ether bonds, O–C–O bonds, and C=O ketone bonds, in ascending binding energy contribution. These correspond to the pink and orange subpeaks. The highest binding energy subpeak, corresponding to the lavender subpeak, was attributed to O=C–O carboxyl bonds and CO_3^{2-} carbonate ions. After irradiation, the area ratios of the pink and orange subpeaks increased despite electron irradiation commonly being associated with an increase in C–C signal due to the deposition and polymerization of hydrocarbons from vacuum pump oil molecules in the SEM. This meant that carbon was not simply deposited on the NW surface as surface hydrocarbons but integrated into the NW chemically. The increase in area ratio for subpeaks associated with carbon–oxygen bonding provided strong evidence that electron irradiation induced the replacement of Zn ions with carbon atoms. This interpretation would corroborate the changes in atomic concentration described above. On the other hand, the lavender subpeak did not display conclusive trends after irradiation, with half of the irradiated locations showing miniscule change in area ratio and the other half showing weak signals at ~ 289 eV binding energy.

For O 1s (Figs. 8(f) and 8(g)), the lowest binding energy subpeak at 529.9 to 530 eV was attributed to ZnO. The remaining subpeaks were analyzed by comparing their area ratios relative to the ZnO subpeak. The subpeaks between 531 and 532 eV were attributed to oxygen bonded to carbon (which is less electronegative than Zn) in configurations such as C–O bonds, O=C–O bonds, and carbonate ions. These carbon–oxygen subpeaks were colored pink and orange to match those shown for carbon–oxygen bonding in C 1s. The highest binding energy subpeak was attributed to adsorbed water molecules. A clear increase in carbon–oxygen related subpeaks was observed, which indicated a decrease in pure ZnO and a possible substitution of Zn ions with carbon atoms. This corroborated the observations from C 1s.

Taken as a whole, the XPS measurements strongly suggest that zinc was removed by electron irradiation and replaced by carbon atoms, while oxygen sites remained largely untouched. This would explain the simultaneous decrease in zinc atomic concentration and increase in carbon atomic concentration while oxygen remained constant. It would also explain the increase in carbon–oxygen bonding observed in both C 1s and O 1s. The increase in binding energy for Zn 2p, while slight, also aligns with the interpretation of zinc removal, which would produce a lower Zn:O ratio and therefore increased de-shielding of Zn electrons. The absence of a zinc carbide signal further provides evidence against the replacement of oxygen atoms with carbon.

The formation of $ZnCO_3$ was ruled out based on the following observations. Firstly, the carbonate signal in C 1s did not provide

convincing evidence of increase after irradiation. For the O 1s, the carbonate signal could feasibly lie within the range of 531–532 eV, which did show an increase after irradiation. However, the lack of correlation with the changes in the C 1s carbonate signal precluded the identification of carbonate. Secondly, the TEM images of the outgrowth did not show characteristics of crystalline $ZnCO_3$ and were in fact amorphous.

3.5 Monte Carlo simulations

To elucidate the electron–matter interactions with ZnO-C, Monte Carlo simulations were conducted in Casino V3.3.0.4 [24]. Simulation parameters are explained in Section 2.

Figures 9(a) and 9(b) show the simulated trajectories of 5 and 20 keV electrons incident on a ZnO-C NW with 200 nm diameter (represented by grey regions), respectively. Figures S7(a)–S7(d) in the ESM show the same images with wider field of view and magnified versions. For clarity, only 200 out of the 10,000 simulated electrons are shown. Blue trajectories indicate the path of primary electrons (PE), i.e., electrons emitted by the electron gun. Red trajectories indicate the path of backscattered electrons (BE), i.e., electrons that ultimately exit the NW from the entry side. Purple trajectories indicate the path of backwards-emitted secondary electrons. Green trajectories indicate secondary electrons generated by PE or BE inside the NW.

For 5 keV PEs, most electrons stop inside the NW. The trajectories inside the NW are also complicated, involving multiple collisions. Additionally, many secondary electrons (SE) are generated. Majority of the SE do not have sufficient energy to leave the NW entirely but have enough energy to move around inside the NW and undergo several collisions before stopping. In practical systems, the accumulated charges are dispersed along the NW length and into the underlying substrate, as mentioned in the discussion of Fig. 2. Comparatively, for 20 keV PEs, most PEs followed trajectories with minimal collisions and deviations and penetrated the entire NW. Secondary electron generation rate was lower than with 5 keV electrons and their subsequent trajectories were also shorter. These results can be understood from the reduced stopping power of electrons in ZnO at 20 keV compared to 5 keV. Figure S8(e) in the ESM shows the stopping power of electrons in ZnO calculated by the ESTAR database [37]. Within the range of 5–20 keV of energies relevant to this work, the stopping power of electrons in ZnO decreases monotonically with electron energy.

To examine the energy absorbed by the NW from electron irradiation, similar Monte Carlo simulations were run for varying combinations of incident electron energy and NW thickness. Absorbed energy was calculated as follows. The sum of total energies of all BE and transmitted electrons (TE) was subtracted

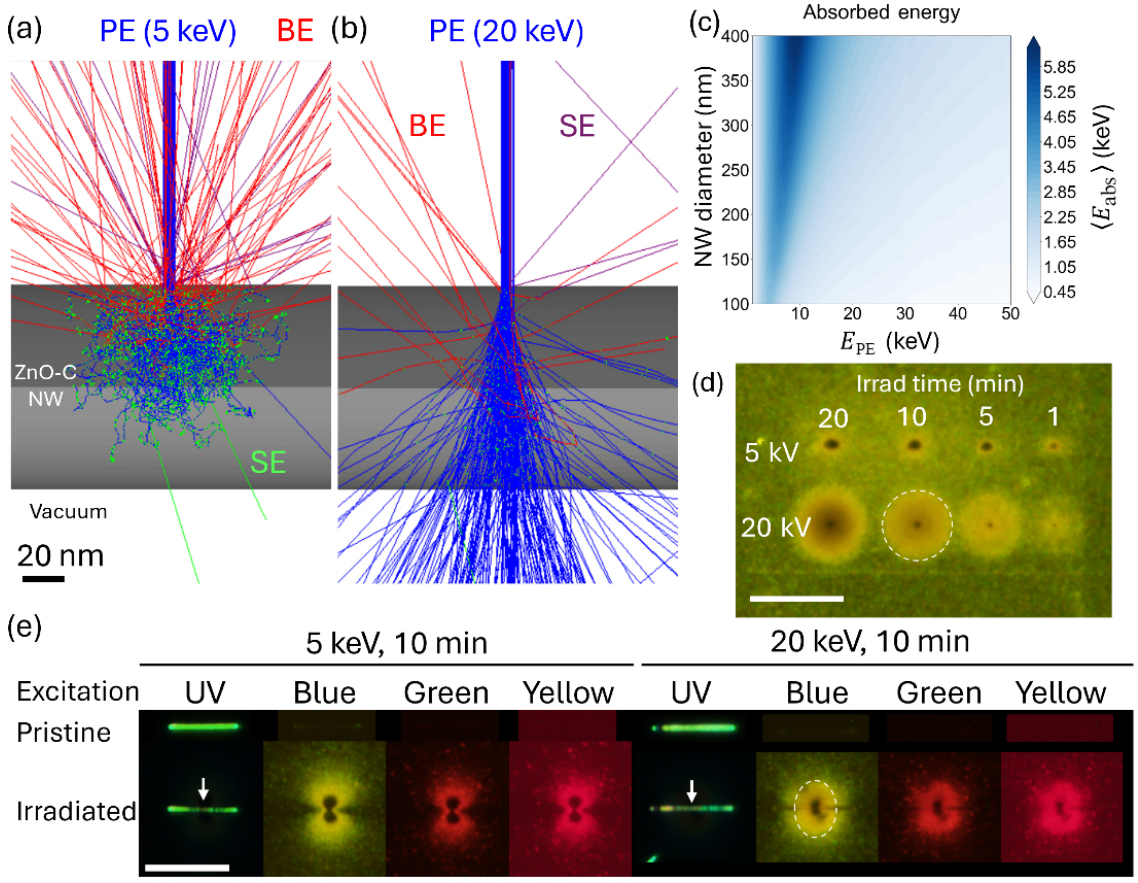

Figure 9 ((a) and (b)) Simulated trajectories of (a) 5 and (b) 20 keV electrons through a freestanding 200 nm ZnO-C NW. White space is vacuum. Grey segments are the ZnO-C NW. Trajectory colors indicate: blue—primary electrons, red—backscattered electrons, green—secondary electrons, and purple—backwards-emitted secondary electrons. (c) Intensity map of average energy absorbed by NW per incident electron $\langle E_{abs} \rangle$ against incident electron energy E_{PE} and NW diameter. (d) Blue light excited FM image of silicon substrate irradiated by 5 and 20 keV electrons for various irradiation times. (e) FM images of two separate Type 1A NWs on silicon substrates under various excitations before and after irradiation by 5 and 20 keV electrons for 10 min, respectively. The white dashed outlines in (d) and (e) show how the halo dimensions compared in the main text were measured. Scale bars: 10 μm.

from the total incident energy of the ensemble of simulated electrons. The resulting value was then divided by the total number of electrons in the ensemble to obtain a representative expectation value of absorbed energy per incident electron for that ensemble. The process was repeated and resulting expectation values were averaged.

Figure 9(c) shows a contour plot of how $\langle E_{abs} \rangle$, the expectation value for energy absorbed per incident PE, varies with NW diameter and initial energy of the PE. Highest energy absorption was observed at the low incident energy range. For 100 nm NWs, maximum energy absorption was 2.9 keV with 4 keV incident energy. For 400 nm NWs, maximum energy absorption was 6.4 keV with 9 keV incident energy. This observation aligns well with Figs. 9(a) and 9(b), which showed that higher energy electrons were more likely to penetrate the NW without fully depositing their energy. It should be noted that while the absorbed energy calculated here represents the average energy delivered by a single electron, the energy would be absorbed over multiple interaction events, such as electron–atom collisions, electron–electron collisions, and secondary electron generation.

Figures 9(a)–9(c) explain the outgrowth height versus incident electron energy trend shown in Fig. 5, where higher incident electron energy led to shorter outgrowths. Mechanistically, EBID is generally understood to occur when electrons cross the solid/vapor phase boundary at the surface of the substrate or deposit. As an electron crosses the surface, it has a probability of decomposing adsorbed precursor molecules into volatile species that then react and form the deposit substance. While different sources disagree on the degree to which each type of electron is responsible for EBID, primary electrons, secondary electrons generated by primary electrons and backscattered electrons, backscattered electrons leaving the substrate and the deposit, and backscattered electrons entering the deposit after leaving the substrate are all believed to be responsible for EBID [34–36]. For EBID on NWs, the reduced penetration and increased energy deposition associated with lower energy energies would result in both secondary electrons and backscattered electrons being generated at higher rates. This can be directly seen from the abundance of red and green trajectories in Fig. 9(a) compared to Fig. 9(b).

Fluorescence microscopy was used to validate the simulation results. Before discussing the results from irradiating NWs, it is useful to establish the fluorescence behavior induced by electron beam interaction with a blank silicon substrate. Figure 9(d) shows the fluorescence patterns under blue excitation for a blank silicon substrate irradiated by various combinations of electron energy and irradiation durations. Optical bright field and FM images taken under green and yellow excitation are also provided in Fig. S9 in the ESM. They show similar patterns. The fluorescent parts of the substrate revealed the path taken by excess electrons as they discharged into the silicon substrate underneath. When unirradiated, the blue FM image of the silicon substrate would be completely dark. Stray low dose irradiation introduced during sample acquisition at low magnification caused enhanced fluorescence of the silicon substrate, as can be seen from the surroundings of the irradiated locations. The enhanced fluorescence could be due to electron-induced formation of fluorescent carbon dots from the surface carbon contamination. Siddique et al. reported excitation wavelength-dependent photoluminescence spectra of carbon dots [38] that were remarkably similar to the excitation-dependent behavior of electron irradiated silicon substrates shown in Fig. S9 in the ESM. The dominant fluorescence color redshifted along with the excitation wavelength such that the color remained at a longer wavelength than the excitation. Furthermore, the fluorescence intensity decreased with red shifts in the excitation wavelength. Moving on, the focal point of the electron beams showed dark spots that correlated with the positions of EBID deposits visible under optical bright field, SEM, and AFM. These were likely due to thick carbon deposits formed from extensive EBID, agglomerating the fluorescent carbon dots into non-fluorescent amorphous bulk carbon. A surrounding "halo" was observed around each focal point with a radial gradient of changing fluorescence intensity, which correlated with the region of carbon inflow and buildup associated with EBID [30, 31, 33–35].

The overall fluorescence intensity was likely to be an interplay of fluorescence enhancement from irradiation of the surface oxidation and darkening due to the non-fluorescent amorphous carbon. At low doses, the substrate fluorescence intensity increases with electron dose. Simultaneously, carbon accumulates due to EBID, causing a competing darkening effect. There exists a turning point where the deposited carbon grows thick enough to reduce the fluorescence intensity. The shape and intensity variation of the fluorescence patterns can thus be used as an indicator of electron distribution as they discharged. A rounder profile was observed for 20 keV electrons because electrons penetrated deeper into the substrate before starting to discharge. The environment inside the substrate is isotropic, hence causing an isotropic electron distribution during discharge. On the other hand, 5 keV electrons deposit most of their energy near the substrate surface, causing increased generation of secondary electrons and backscattered electrons that have been shown to be directly involved in the EBID mechanism [34–36], thereby producing larger dark spots of carbon buildup. The electron distribution shape would thus match the SEM scanning pattern more closely, which was a horizontal rectangle in this case. Supposing that longer irradiation durations can be associated with greater total energy deposited in the substrate, the size of the halo can also be used as an indicator of the quantity of energy deposited.

Figure 9(e) shows fluorescence micrographs that validate the simulated trajectories in NWs. Two separate Type 1A NWs were dry transferred to a blank silicon substrate and irradiated with 5 and 20 keV electron beams at high magnification, respectively. Under UV excitation, the NWs exhibit quenched green fluorescence as expected. However, blue, green, and yellow excitation are not sufficiently energetic to excite electrons across the 3.37 eV band gap of ZnO. The NW thus mostly appears transparent under visible wavelength excitations when pristine, barring mild scattering effects showing parts of the NW. However, visible wavelength fluorescence of the underlying substrate can still be seen as ZnO is optically transparent. After irradiation, the fluorescence patterns of the substrate under the NW irradiated by 20 keV electrons were similar to that seen for the blank substrate, supporting the interpretation that majority of PEs penetrated the entire NW and formed the round halo in the substrate as if the NW was absent. Comparing the observations for 10 min of 20 keV electron energy irradiation, the halo in the blank substrate was radially symmetric with a diameter of 7.3 μm while the halo under the irradiated NW was elliptical with a major axis of 6.0 μm perpendicular to the NW and minor axis of 4.6 μm parallel to the NW. The smaller halo under the NW indicated that less energy was deposited into the silicon substrate due to energy being absorbed by

the NW, corroborating the simulation results. Furthermore, the dark spot indicative of direct electron irradiation had a larger radius here than it did for the blank silicon substrate shown in Fig. 9(d), which corroborated the widening of electron trajectories into a cone, as shown in Fig. 9(b). Closer inspection of the dark spot revealed that the spot extended further perpendicular to the NW than parallel, an effect that will be discussed below.

Comparatively, after 5 keV electron irradiation, the substrate's fluorescence pattern exhibited a bloom pattern. The dark spot indicative of direct electron irradiation extended perpendicularly outwards from the NW (above and below the NW with respect to the image) further than they did for 20 keV electrons. The direct irradiation of the substrate above and below the NW was likely due to electrons that entered the NW nearer the edge of the NW and experienced collisions that diverted their trajectory out the side walls of the NW. Due to the increased interaction cross section for lower energy electrons, trajectory diversions experienced by 5 keV electrons were greater than that for 20 keV electrons, as demonstrated above by the Casino simulations. This trajectory broadening was also likely to be responsible for the wider outgrowth base associated with lower electron energies shown in Fig. 5(c). Notably, the parts of the substrate directly under the NW (i.e., parallel to the NW) showed a constriction of the dark spot and minimal fluorescence enhancement. This was because the electrons that stopped inside the NW would flow lengthwise along the NW, dispersing into the substrate across a broader region. This matches the interpretation of Figs. 2(d) and 2(e).

4 Discussion

4.1 Mechanism for LEE interaction with ZnO-C

Synthesizing the XPS and Monte Carlo simulation results, the electron irradiation-induced reduction of zinc concentration can now be explained. There are three explanations for the reduction in zinc, all of which most likely occur simultaneously. Firstly, the scattering cross section for zinc is higher than that for oxygen. For example, for 1 keV incident electrons, the elastic scattering cross section for zinc is 1.35×10^{-16} cm^2 [39] while that for atomic oxygen is approximately 0.5×10^{-16} cm^2 [40, 41]. Therefore, there is a higher probability for primary electrons to scatter off zinc atoms than oxygen. Furthermore, in ZnO, zinc atoms have a lower displacement energy barrier than oxygen atoms (18.5 eV for zinc compared to 41.4 eV for oxygen) [42]. Assuming head-on collisions in the formula presented by Bradley and Zaluzec [43], the maximum energy transferred from electron to zinc nuclei was calculated to be 0.17 eV for 5 keV electrons and 0.68 eV for 20 keV electrons. The maximum energy transferred to oxygen nuclei was 0.69 eV for 5 keV electrons and 2.8 eV for 20 keV electrons. Clearly, single collisions between electron and nuclei cannot overcome the displacement barrier. Nonetheless, the simulated trajectories in Figs. 9(a) and 9(b) show that collisions would be abundant. The simulation results in Fig. 9(c) also showed that within the range of 5–20 keV of incident electron energy, the average energy deposited per incident electron was on the order of 1 to 5 keV. While the energy would be deposited over multiple interaction events, the high dose rate of electrons (on the order of 10^8 to 10^{10} e$^-$·s^{-1}) would make it possible for multiple simultaneous electron collisions to supply sufficient energy to displace atoms. Since zinc atoms have a lower displacement energy than oxygen, zinc would be removed at a higher rate.

Secondly, electron-induced radiolysis in oxides has been found to primarily result in oxygen ionization [44]. Combined with the generation of neutral and positively-charged oxygen atoms via the Knotek–Feibelmann (KF) mechanism (which is applicable for maximally valent transition metal oxides like ZnO) [45], oxygen ions can be ejected from the sample surface. Each lost surface oxygen leaves behind up to three loosely bound surface zinc atoms which can stabilize by moving to interstitial positions. Zinc interstitials have been calculated to have low migration barriers at 0.78 eV for motion along the <0001> axis, 0.90 eV for motion perpendicular to the <0001> axis, and 0.57 eV for an isotropic kick-out mechanism involving a zinc substitutional defect [46]. They are mobile even at room temperature and are easily displaced with energy provided by electron irradiation. Each lost oxygen atom thus causes further zinc depletion.

Thirdly, XPS signals originate from approximately 5 nm or less from the surface, which is much shorter than the thickness of outgrowths produced under extended irradiation. As shown in Fig. 4(c), even just 1 min of irradiation could produce a 30 nm thick outgrowth. These carbon-dominated outgrowths would block the Zn signal from the NW underneath. Figure S10 in the ESM shows EDX elemental maps of the largest outgrowth from the NW in Fig. 4(f) captured using 5 keV electrons and 20 keV electrons. The Zn and O maps showed reduced signal in the outgrowth when captured with 5 keV electrons compared to 20 keV electrons. This demonstrates how the EBID outgrowth, which was approximately 500 nm thick in this case, can block signals from the underlying ZnO NB due to the reduced penetration of lower energy electrons, which can contribute to the reduced Zn atomic concentration detected through XPS. The O map also showed a lower degree of reduced signal than the Zn map, which algins with the atomic concentration results measured by XPS, where zinc was reduced while oxygen concentration remained approximately the same. Nonetheless, it should also be noted that this explanation would have a relatively small contribution to the XPS results due to the X-ray probe (spot size of approximately 110 μm) being significantly larger than the typical lateral size of outgrowths (less than 1 μm) and the distance between well-formed outgrowths in the ZnO-C array sample being on the order of a few micrometers.

4.2 Mechanism for fluorescence modifications

The quenching of the polarized yellow emission in Type 1B and Type 2B NWs could be understood as follows. It was found in Ref. [21] that a C_O-V_O defect complex was responsible for the yellow emission. Based on the partial density of states, approximately half of the electronic transitions responsible for the emission were due to a de-excitation from zinc d-orbitals to carbon p-orbitals, or in other words, electron transfer between zinc and carbon. A key feature of the defect was a shortened bond length between the C_O atom and a neighboring zinc atom, which implied strong zinc–carbon interaction between those two atoms and therefore the location of the electron transfer. Crucially, the perpendicular polarization of the emission arose because the preferential orientation between the zinc and C_O atoms was such that the two atoms lay in a horizontal plane perpendicular to the growth of the ZnO NW. The removal of zinc via electron irradiation, as suggested by XPS results, would thus disrupt the emissive properties of the C_O-V_O defect, causing the yellow emission to be quenched.

The green emissions in Type 1A NWs are most likely due to multiple species of randomly oriented defects. In literature, many defect species have been proposed to be responsible for green fluorescence, including native defects in various charged states like oxygen vacancies, oxygen interstitials, zinc vacancies, and zinc interstitials, and unintentional impurities like hydrogen, carbon, gold, and copper introduced during fabrication [1]. For the NWs studied in this work, native defects and carbon-containing defects are the most plausible. Realistically, multiple defect species are simultaneously responsible for the green emission as the emission spectrum is broadband and asymmetric, as can be seen from Fig. S11(b) in the ESM. In contrast with the regularly oriented C_O-V_O defect complex responsible for yellow emissions, the point defects responsible for green emission do not have preferred orientations. Therefore, even if the defect atoms migrate due to electromigration, they can continue acting as emission centres. The parts of the NW that exhibit fluorescence quenching are likely due to the disruption of defect complexes that consist of multiple defects. Compared to the green fluorescence in Type 1A NWs, the red fluorescence in Type 2A NWs is associated with higher carbon concentrations [17, 22]. These carbon impurities act as scattering centres that hinder the lengthwise flow of electrons along the NW. This explains why Type 2A NWs displayed less distinct modifications over shorter spatial lengths compared to Type 1A NWs. Nonetheless, electron irradiation likely also caused beam heating from direct irradiation and Joule heating from lengthwise electron flow. This would have produced a mild annealing effect that removed charge-trapping defects and reduced non-radiative recombination pathways, enhancing the fluorescence intensity. This could account for why fluorescence enhancement was observed even at low electron doses (leftmost column of Fig. 3(a)).

At high probe currents, localized fluorescence quenching and fluorescence color conversion from red to green were observed. Localized fluorescence quenching could be attributed to two effects. Firstly, high electron current supplied sufficient energy to enable the electromigration of carbon in the NW bulk away from the irradiated spot. Secondly, sufficiently high probe current caused EBIE to dominate over EBID. This was shown by the stark brightness contrast in the SEM image in Fig. 3(c) between the locations irradiated by different probe currents. It was also shown by the relative flatness of the irradiated area in Fig. 4(e). Such etching could cause a reduction in surface carbon. These two effects would disrupt the carbon-heavy defect species that are responsible for red emissions.

The reduction of carbon in the NW bulk due to electromigration was also responsible for the color conversion from red to green. Figure S11(d) in the ESM shows additional fluorescence spectra characterization that was performed on the Type 2A NW in Fig. 1(c). The color conversion from red to green was reflected in the spectra by a greater increase in spectral intensity at higher energy above 2.3 eV. Consulting past calculations by Lim et al. and Lu et al. for energetically stable defect complexes in ZnO-C that are optically relevant [17, 22], it is possible to hypothesize the conversion of defect species responsible for the color conversion. Defects that could be responsible for red emissions in the energy range of 1.80–1.90 eV are $2C_O$-Zn_i, $3C_O$, and $2C_O$-V_O-Zn_i. The defect that could be responsible for the green emissions (2.31 eV) is C_O-Zn_i. A color conversion from red to green could thus be explained by a decrease in C_O defects which aligns with the hypothesis that electromigration of carbon away from the irradiated spot was responsible for the modifications. One other notable observation was that the areas surrounding the irradiated spot showed darkening in the SEM image (Fig. 3(c)) and increased thickness (Fig. 4(e)). These characteristics are well-understood to indicate carbon deposits formed from the inflow of carbon towards the etched area [30, 31, 33–35]. These locations with surface carbon deposits also lined up with the locations where defect fluorescence was converted to green color, which could suggest that the modification of surface states on the NW by a layer of amorphous carbon plays a role in explaining the color conversion as well. However, this requires additional study.

The bulk-to-surface distribution of defects in any given NW was deducible from the spatial distribution of fluorescence modifications. The fluorescence modifications were driven by flow of electrons both in the bulk and on the surface of the NWs. Evidence of bulk electron flow was shown in Figs. 2(d) and 2(e). The substrate fluorescence patterns introduced in Fig. 9(d) were used to demonstrate surface electron flow modifying the NW fluorescence. Under the reasonable assumption that the distribution of electrons flowing in the bulk and on the surface of the NW was approximately the same for all NWs of the same type, the degree of match between the NW fluorescence quenching length and the substrate fluorescence pattern revealed the distribution of defects in the NW. A close match between the NW quenching length and substrate fluorescence pattern size implied that defects were concentrated on NW surface. This analysis was elaborated in Figs. S12 and S13 in the ESM.

4.3 Mechanism for EBID on ZnO-C NWs

In the initial stages of irradiation, zinc is removed by electron irradiation and replaced by the inflow of carbon from surface contamination. The deposited carbon bonds with the remaining oxygen, forming an amorphous carbon-oxygen hybrid as the outgrowth grows thicker. Evidence of carbon–oxygen bonding was demonstrated by XPS results in Fig. 8. While carbon deposition from residual vacuum hydrocarbons cannot be ruled out entirely, observations over multiple samples of varying ages suggested that ease of EBID was more related to surface contamination and possibly differences in carbon content between NWs than vacuum contamination. This was based on observations that NWs on different parts of the same substrate would produce outgrowths at different rates despite being irradiated in the same chamber within minutes of each other. As the outgrowth thickness increases, oxygen availability from the NW would decrease. This was demonstrated by Fig. 6(f) where the oxygen elemental map lacked spatial correlation with the "N"-shaped deposit. The outgrowth would thus transition to a carbon-dominated surface deposition. The carbon layer was amorphous, as shown by the side-view high-resolution TEM (HRTEM) image of a deposit in Fig. 7(c) and the corresponding FFT in Fig. 7(d). Repeated TEM observations of additional samples shown in Fig. S6 in the ESM similarly showed that the deposits acted as an amorphous layer covering the NW. The topmost layer was relatively loosely bound, as demonstrated by laser ablation experiments shown in Fig. S14 in the ESM. In sum, as the outgrowth is formed, the composition transitions from ZnO-C to Zn_{1-x}O-C to C-O to amorphous carbon. Figure S15 in the ESM shows additional TEM images of the boundary region at the edge of a carbon deposit, which provided further evidence for this gradual transition from crystalline to amorphous composition.

4.4 Electron discharge pathways

Examining fluorescence images after electron irradiation in tandem with SEM observations during irradiation, the fluorescence patterns caused by electron irradiation were interpreted as follows. Fluorescence enhancement was an indicator of surface oxide removal, while dark patches indicated EBID of carbon. During irradiation of NWs supported by silicon substrate, the electrons must discharge downwards into the silicon substrate because the electrical contact with the metallic sample holder was through a piece of carbon tape on the underside of the substrate. However, if electron discharge rate was slower than the rate of incoming electrons, substrate charging or electron pileup would occur. This causes the electrons to spread out laterally over the substrate surface to discharge over a wider radius and hinders the flow of additional electrons into the area.

It was noted that similar patterns were observed between SEM image darkening associated with substrate charging and the fluorescence patterns like those shown in Fig. 9, meaning that the pileup radius could be visualized with fluorescence imaging. For a given electron energy, the radius likely increases with probe current and surface conductivity while decreasing with bulk conductivity. With a high bulk conductivity to probe current ratio, electrons would flow through the substrate easily, and the fluorescence patterns would be largely attributable to dispersion of the primary electrons in the substrate. With a lower ratio, more electrons would flow laterally outwards from the irradiated point along the substrate surface such that discharge occurs over a wider cross-sectional area. However, the unavoidable presence of surface oxidation would reduce the surface conductivity and restrict the surface flow of electrons as well. An equilibrium would be set up depending on the bulk conductivity, surface conductivity, and probe current that determined the pileup radius. When a segment of a NW was present within the pileup radius, the fluorescence of that segment was modified as well. This explains why probe current influenced the spatial length of fluorescence modification in NWs that were directly irradiated and why proximate Type 1A NWs displayed fluorescence quenching despite not being directly irradiated.

Simultaneously, the interaction between electrons and surface oxidation would reduce the oxide layer, improving the surface conductivity over time. This would explain why the pileup radius increased with irradiation duration. As mentioned in the discussion of Fig. 2(a), each irradiation interval improved the surface conductivity. When the NW was removed from the SEM, the electron pileup was able to completely discharge with the help of ambient moisture. Surface re-oxidation would have required a longer timescale. This meant that in subsequent irradiations, the electron pileup radius and thus NW fluorescence quenching length would increase to a larger value before equilibrium was reached.

5 Conclusions

The defect fluorescence of ZnO-C NWs was modified with sub-micron precision via localized irradiation by 5–20 keV electrons at high magnification, enabling intra-NW fluorescence patterning. Type 1A NWs characterized by green defect fluorescence displayed heterogeneous fluorescence quenching upon electron irradiation. Type 1A NWs were found to be highly sensitive to contact with electrons, displaying fluorescence quenching due to the presence of electrons discharging through the substrate under them even when not directly irradiated. Type 2A NWs characterized by elevated carbon content and red defect fluorescence exhibited fluorescence enhancement at low doses of electron irradiation. Fluorescence quenching was observed at high doses but was much more localized compared to Type 1A NWs. Additionally, color conversion from red to green was observed in some samples, particularly at higher probe currents. The additional polarized yellow defect emissions present in Type 1B and Type 2B NWs displayed more localized and higher degree of quenching compared to the unpolarized emissions. For all four types of NWs, electron dose and electron dose rate (controlled by probe current) were found to be the most significant parameters that controlled the magnitude of fluorescence intensity modification and spatial extent of modification.

Additionally, at longer irradiation durations, EBID of amorphous carbon was observed, causing material outgrowth on NWs whose size, shape, and position could be precisely controlled by SEM operation. It was found that longer irradiation durations and lower probe current produced taller outgrowths. Probe current, and to a smaller extent electron energy, were also found to control outgrowth shape.

XPS analysis revealed that electron irradiation of ZnO-C induced the replacement of zinc ions by carbon. The trajectory of electrons through the NW during irradiation was elucidated by Monte Carlo simulations and visualized by fluorescence microscopy. Electrons with lower energy stop completely in the NW, depositing most of their energy inside the NW with greater dispersion. Electrons were then discharged by flowing to either ends of the NWs or directly into the substrate under the irradiated spot if a substrate was present. Electron pileup caused discharging electrons to spread out over the substrate surface in a radius that was determined by substrate bulk conductivity, surface oxidation, electron dose rate, electron dose, and electron energy.

Electronic Supplementary Material: Supplementary material (FM and OM micrographs of nanowires used to construct Fig. 2(a); FM, OM, and SEM images that demonstrate electron flow lengthwise along nanowires and proximity quenching effect; timelapse images showing EBID and EBIE on the NW in Fig. 4(e); additional NW displaying etching-dominated deposit growth; additional AFM characterization of the NW shown in Fig. 4(f); additional TEM images of EBID outgrowths; summary of XPS peak area ratios for other electron-irradiated regions; alternate fields of view of the simulated electron trajectories shown in Figs. 9(a) and 9(b); additional FM and OM images of electron-irradiated silicon substrates with other excitation wavelengths; EDX elemental maps of the largest EBID outgrowth on the NW in Fig. 4(f) captured with different electron energies; additional fluorescence spectra characterization of electron-irradiated Type 1A and Type 2A nanowires; fluorescence image comparisons between length of NW fluorescence modification and substrate fluorescence pattern; AFM measurements of height and shape change of the largest EBID outgrowth on the NW in Fig. 4(f) upon irradiation by 325 nm laser at various laser powers; and TEM image of boundary region at the edge of EBID deposit) is available in the online version of this article at https://doi.org/10.26599/NR.2026.94908866.

Data availability

All data needed to support the conclusions in the paper are presented in the manuscript and the Electronic Supplementary

Material. Additional data related to this paper may be requested from the corresponding author upon request.

Acknowledgements

J. K. K. acknowledges the generous support from the National University of Singapore Graduate Tutor Scheme. C. H. S. acknowledges the generous support from the National University of Singapore Faculty of Science (No. E14100009101).

Declaration of competing interest

All the contributing authors report no conflict of interests in this work.

Author contribution statement

J. K. K. Conceptualization, methodology, investigation, validation, formal analysis, writing – original draft, writing – review & editing, visualization. K. Y. L. Conceptualization, methodology, resources, investigation, writing – review & editing, supervision. D. L. S. H. Investigation, data curation. C. H. S. Conceptualization, methodology, resources, supervision, writing – review & editing, project administration, funding acquistion. All the authors have approved the final manuscript.

Use of AI statement

None.

References

[1] Galdámez-Martinez, A.; Santana, G.; Güell, F.; Martínez-Alanis, P. R.; Dutt, A. Photoluminescence of Zno nanowires: A review. *Nanomaterials* **2020**, *10*, 857.

[2] Rasmidi, R.; Duinong, M.; Chee, F. P. Radiation damage effects on zinc oxide (ZnO) based semiconductor devices—A review. *Radiat. Phys. Chem.* **2021**, *184*, 109455.

[3] Klochko, N. P.; Klepikova, K. S.; Petrushenko, S. I.; Dukarov, S. V.; Kopach, V. R.; Khrypunova, I. V.; Zhadan, D. O.; Lyubov, V. M.; Khrypunova, A. L. Effect of high doses of electron beam irradiation on structure and composition of ZnO films prepared by electrochemical and wet chemical depositions on solid and flexible substrates. *Radiat. Phys. Chem.* **2019**, *164*, 108380.

[4] Borysiewicz, M. A. ZnO as a functional material, a review. *Crystals* **2019**, *9*, 505.

[5] Ding, M.; Guo, Z.; Zhou, L. Q.; Fang, X.; Zhang, L. L.; Zeng, L. Y.; Xie, L. A.; Zhao, H. B. One-dimensional zinc oxide nanomaterials for application in high-performance advanced optoelectronic devices. *Crystals* **2018**, *8*, 223.

[6] Janotti, A.; Van de Walle, C. G. Fundamentals of zinc oxide as a semiconductor. *Rep. Prog. Phys.* **2009**, *72*, 126501.

[7] Xu, X.; Li, D. X.; Yuan, J.; Zhou, Y. H.; Zou, Y. P. Recent advances in stability of organic solar cells. *EnergyChem* **2021**, *3*, 100046.

[8] Zhang, Y.; Nayak, T. R.; Hong, H.; Cai, W. Biomedical applications of zinc oxide nanomaterials. *Curr. Mol. Med.* **2013**, *13*, 1633–1645.

[9] In, J. B.; Kwon, H. J.; Lee, D.; Ko, S. H.; Grigoropoulos, C. P. *In situ* monitoring of laser-assisted hydrothermal growth of ZnO nanowires: Thermally deactivating growth kinetics. *Small* **2014**, *10*, 741–749.

[10] Hong, S.; Yeo, J.; Manorotkul, W.; Kim, G.; Kwon, J.; An, K.; Ko, S. H. Low-temperature rapid fabrication of ZnO nanowire UV sensor array by laser-induced local hydrothermal growth. *J. Nanomater.* **2013**, *2013*, 246328.

[11] Lee, H.; Manorotkul, W.; Lee, J.; Kwon, J.; Suh, Y. D.; Paeng, D.; Grigoropoulos, C. P.; Han, S.; Hong, S.; Yeo, J. et al. Nanowire-on-nanowire: All-nanowire electronics by on-demand selective integration of hierarchical heterogeneous nanowires. *ACS Nano* **2017**, *11*, 12311–12317.

[12] Yeo, J.; Hong, S.; Kim, G.; Lee, H.; Suh, Y. D.; Park, I.; Grigoropoulos, C. P.; Ko, S. H. Laser-induced hydrothermal growth of heterogeneous metal-oxide nanowire on flexible substrate by laser absorption layer design. *ACS Nano* **2015**, *9*, 6059–6068.

[13] Fujii, S.; Fukano, R.; Hayami, Y.; Ozawa, H.; Muneyuki, E.; Kitamura, N.; Haga, M. A. Simultaneous formation and spatial patterning of ZnO on ITO surfaces by local laser-induced generation of microbubbles in aqueous solutions of $[Zn(NH_3)_4]^{2+}$. *ACS Appl. Mater. Interfaces* **2017**, *9*, 8413–8419.

[14] Soci, C.; Zhang, A.; Bao, X. Y.; Kim, H.; Lo, Y.; Wang, D. Nanowire photodetectors. *J. Nanosci. Nanotechnol.* **2010**, *10*, 1430–1449.

[15] Cui, J. B. Zinc oxide nanowires. *Mater. Charact.* **2012**, *64*, 43–52.

[16] Wilson, H. F.; Tang, C. G.; Barnard, A. S. Morphology of zinc oxide nanoparticles and nanowires: Role of surface and edge energies. *J. Phys. Chem. C* **2016**, *120*, 9498–9505.

[17] Lim, K. Y.; Linghu, J.; Chi, X.; Yuan, K. D.; Hew, K. M.; Zheng, M. R.; Yang, M.; Tok, E. S.; Rusydi, A.; Yu, X. J. et al. Tunable fluorescence properties due to carbon incorporation in zinc oxide nanowires. *Adv. Opt. Mater.* **2017**, *5*, 1700381.

[18] Chua, S. T.; Lim, K. Y.; Zhang, Z.; Sow, C. H. Selective micro laser annealing for fluorescence tuning of carbon-incorporated zinc oxide nanowire arrays. *J. Mater. Chem. C* **2019**, *7*, 6279–6288.

[19] Bah, A.; Lim, K. Y.; Wei, F. H.; Khursheed, A.; Sow, C. H. Fluorescence invigoration in carbon-incorporated zinc oxide nanowires from passage of field emission electrons. *Sci. Rep.* **2019**, *9*, 9671.

[20] Sow, B. M.; Lim, K. Y.; Wu, J. F.; Sow, C. H. Electrically tailored metachrosis in ZnO-C nanowires. *ACS Nano* **2020**, *14*, 5845–5854.

[21] Kang, J. K.; Lim, K. Y.; Sow, C. H. Emission wavelength selection via anomalous polarized fluorescence in ZnO-C nanowires. *Nano Res.* **2024**, *17*, 4489–4497.

[22] Lu, Y. H.; Hong, Z. X.; Feng, Y. P.; Russo, S. P. Roles of carbon in light emission of ZnO. *Appl. Phys. Lett.* **2010**, *96*, 091914.

[23] Kerherve, G.; Kerherve, E.; Skinner, W. *KherveFitting* [Online]. https://sourceforge.net/projects/khervefitting/ (accessed Apr 6, 2025).

[24] Demers, H.; Poirier-Demers, N.; Couture, A. R.; Joly, D.; Guilmain, M.; De Jonge, N.; Drouin, D. Three-dimensional electron microscopy simulation with the CASINO Monte Carlo software. *Scanning* **2011**, *33*, 135–146.

[25] Lide, D. R. *CRC Handbook of Chemistry and Physics: A Ready-Reference of Chemical and Physical Data*; CRC Press: Boca Raton, 2004.

[26] Schmidt-Mende, L.; MacManus-Driscoll, J. L. ZnO-nanostructures, defects, and devices. *Mater. Today* **2007**, *10*, 40–48.

[27] Hengehold, R. L.; Almassy, R. J.; Pedrotti, F. L. Electron energy-loss and ultraviolet-reflectivity spectra of crystalline ZnO. *Phys. Rev. B* **1970**, *1*, 4784–4791.

[28] Dorn, R.; Lüth, H. Single and multiple excitation of bulk and surface plasmons on clean ZnO surfaces. *J. Appl. Phys.* **1976**, *47*, 5097–5098.

[29] Kikuchi, S.; Takahashi, Y.; Sakata, T. Measurement on work function of polycrystalline zinc oxide covered by organic dye. *Appl. Opt.* **1969**, *8*, 42–44.

[30] Hugenschmidt, M.; Adrion, K.; Marx, A.; Müller, E.; Gerthsen, D. Electron-beam-induced carbon contamination in STEM-in-SEM: Quantification and mitigation. *Microsc. Microanal.* **2023**, *29*, 219–234.

[31] Mitchell, D. R. G. Contamination mitigation strategies for scanning transmission electron microscopy. *Micron* **2015**, *73*, 36–46.

[32] Roediger, P.; Wanzenboeck, H. D.; Hochleitner, G.; Bertagnolli, E. Evaluation of chamber contamination in a scanning electron microscope. *J. Vac. Sci. Technol. B* **2009**, *27*, 2711–2717.
[33] Hirsch, P.; Kässens, M.; Püttmann, M.; Reimer, L. Contamination in a scanning electron microscope and the influence of specimen cooling. *Scanning* **1994**, *16*, 101–110.
[34] Van Dorp, W. F.; Hagen, C. W. A critical literature review of focused electron beam induced deposition. *J. Appl. Phys.* **2008**, *104*, 081301.
[35] Randolph, S. J.; Fowlkes, J. D.; Rack, P. D. Focused, nanoscale electron-beam-induced deposition and etching. *Crit. Rev. Solid State Mater. Sci.* **2006**, *31*, 55–89.
[36] Fowlkes, J. D.; Randolph, S. J.; Rack, P. D. Growth and simulation of high-aspect ratio nanopillars by primary and secondary electron-induced deposition. *J. Vac. Sci. Technol. B* **2005**, *23*, 2825–2832.
[37] Berger, M. J. *ESTAR, PSTAR, ASTAR. A PC Package for Calculating Stopping Powers and Ranges of Electrons, Protons and Helium Ions. Version 2*. International Atomic Energy Agency: Vienna. 1993.
[38] Siddique, A. B.; Pramanick, A. K.; Chatterjee, S.; Ray, M. Amorphous carbon dots and their remarkable ability to detect 2,4,6-trinitrophenol. *Sci. Rep.* **2018**, *8*, 9770.
[39] McEachran, R. P.; Marinković, B. P.; García, G.; White, R. D.; Stokes, P. W.; Jones, D. B.; Brunger, M. J. Integral cross sections for electron–zinc scattering over a broad energy range (0.01–5000 eV). *J. Phys. Chem. Ref. Data* **2020**, *49*, 013102.
[40] Alves, L. L.; Coche, P.; Ridenti, M. A.; Guerra, V. Electron scattering cross sections for the modelling of oxygen-containing plasmas*. *Eur. Phys. J. D* **2016**, *70*, 124.
[41] Itikawa, Y.; Ichimura, A. Cross sections for collisions of electrons and photons with atomic oxygen. *J. Phys. Chem. Ref. Data* **1990**, *19*, 637–651.
[42] Zhan, J. H.; Bando, Y.; Hu, J. Q.; Golberg, D. Nanofabrication on ZnO nanowires. *Appl. Phys. Lett.* **2006**, *89*, 243111.
[43] Bradley, C. R.; Zaluzec, N. J. Atomic sputtering in the analytical electron microscope. *Ultramicroscopy* **1989**, *28*, 335–338.
[44] Jiang, N. Electron beam damage in oxides: A review. *Rep. Prog. Phys.* **2015**, *79*, 016501.
[45] Knotek, M. L.; Feibelman, P. J. Ion desorption by core–hole auger decay. *Phys. Rev. Lett.* **1978**, *40*, 964–967.
[46] Janotti, A.; Van de Walle, C. G. Native point defects in ZnO. *Phys. Rev. B* **2007**, *76*, 165202.